RESEARCH ARTICLE SUMMARY

ENZYMOLOGY

Revealing enzyme functional architecture via high-throughput microfluidic enzyme kinetics

C. J. Markin†, D. A. Mokhtari†, F. Sunden, M. J. Appel, E. Akiva, S. A. Longwell, C. Sabatti, D. Herschlag*, P. M. Fordyce*

INTRODUCTION: Enzymes possess extraordinary catalytic proficiency and specificity. These properties ultimately derive from interactions not just between the active-site residues and the substrate but from functional interactions throughout a folded enzyme. Therefore, understanding the origins of catalytic proficiency and specificity will require the ability to make mutations throughout the protein. Traditionally, enzyme active sites have been characterized by means of site-directed mutagenesis (SDM), revealing much about the catalytic functions of these residues; nevertheless, SDM is low-throughput, costly, and labor intensive. By contrast, recently developed high-throughput mutational scanning techniques assay large numbers of sequences but provide only coarse estimates of function, such as the amount of product generated at a particular time under a particular set of conditions or overall organismal fitness.

RATIONALE: New technologies are needed to overcome the limitations of current approaches and allow deep characterization of many enzyme variants in a cost- and time-efficient manner. To meet this challenge, we developed a high-throughput microfluidic platform that allows the simultaneous expression and purification of more than 1500 rationally chosen enzyme mutants in hours and allows their quantitative functional characterization in days. HT-MEK (High-Throughput Microfluidic Enzyme Kinetics) can be used with any enzyme system that can be tagged and expressed in vitro and has a direct or coupled fluorogenic assay.

RESULTS: As a first application of HT-MEK, we functionally characterized 1036 single-site mutants that contain either a glycine or valine substitution at each position within PafA (phosphate-irrepressible alkaline phosphatase of Flavobacterium), a well-studied enzyme from the alkaline phosphatase superfamily. For each mutant, we measured Michaelis-Menten kinetics [apparent unimolecular rate constant (k_{cat}), Michaelis constant (K_m), and k_{cat}/K_m] for multiple substrates, inhibition constants, and effects on folding, obtaining more than 5000 kinetic and thermodynamic constants from more than 670,000 total reactions. We found that most mutations (702 of 1036) yielded statistically significant effects on some aspect of catalysis. By systematically and independently varying expression and assay conditions, we determined that 232 of these mutations reduced catalysis by promoting the formation of a long-lived, catalytically inactive misfolded state, whereas none did so through equilibrium unfolding under our assay conditions. Combining these functional measurements with prior mechanistic knowledge allowed us to systematically assess the effect of each mutation. Different groups of residues affected different aspects of function, with residues that affect a particular function forming large, spatially contiguous regions that spanned from the active site up to 20 Å from the active site and to the enzyme surface.

CONCLUSION: HT-MEK has allowed us to uncover functional effects throughout PafA and to identify the catalytic features affected by different groups of residues. Some of these effects are readily rationalized through inspection of structural interconnections to the active site, whereas others were nonobvious, including large distal and surface effects and the discovery of a long-lived misfolded state. These results underscore the need to measure the effects of mutations on multiple kinetic and thermodynamic parameters across multiple reaction conditions and thus the need for this new technology. Because HT-MEK is applicable to any enzyme with a direct or coupled fluorescent readout and provides an in-depth and quantitative analysis of mutant space rapidly and at modest cost, it may be the method of choice to characterize new enzymes. In future applications, HT-MEK can be used to dissect potential evolutionary trajectories, determine the functional consequences of human disease-associated allelic variants, identify surfaces with nascent allosteric potential for rational control of catalysis, and direct the adaptation of natural and designed enzymes for new functions and roles. ■

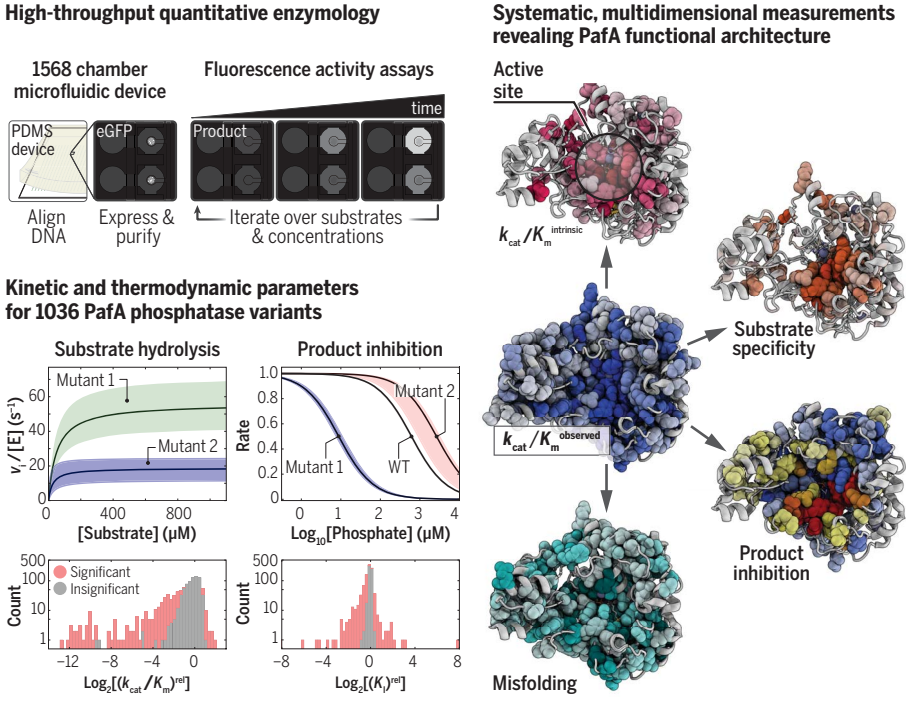

Simultaneous expression, purification, and biochemical characterization of enzyme variants in a microfluidic device makes it possible to measure Michaelis-Menten parameters and inhibition constants for more than 1500 variants in days. Mutational effects across multiple assays reveal an extensive functional architecture in which physically contiguous residue regions extending to the enzyme surface control or alter particular aspects of catalysis.

The list of author affiliations is available in the full article online.
*Corresponding author. Email: herschla@stanford.edu (D.H.); pfordyce@stanford.edu (P.M.F.)
†These authors contributed equally to this work.
Cite this article as C. J. Markin *et al.*, *Science* **373**, eabf8761 (2021). DOI: 10.1126/science.abf8761

READ THE FULL ARTICLE AT
https://doi.org/10.1126/science.abf8761

RESEARCH ARTICLE

ENZYMOLOGY

Revealing enzyme functional architecture via high-throughput microfluidic enzyme kinetics

C. J. Markin[1]†, D. A. Mokhtari[1]†, F. Sunden[1], M. J. Appel[1], E. Akiva[2], S. A. Longwell[3], C. Sabatti[4,5], D. Herschlag[1,6,7]*, P. M. Fordyce[3,7,8,9]*

Systematic and extensive investigation of enzymes is needed to understand their extraordinary efficiency and meet current challenges in medicine and engineering. We present HT-MEK (High-Throughput Microfluidic Enzyme Kinetics), a microfluidic platform for high-throughput expression, purification, and characterization of more than 1500 enzyme variants per experiment. For 1036 mutants of the alkaline phosphatase PafA (phosphate-irrepressible alkaline phosphatase of Flavobacterium), we performed more than 670,000 reactions and determined more than 5000 kinetic and physical constants for multiple substrates and inhibitors. We uncovered extensive kinetic partitioning to a misfolded state and isolated catalytic effects, revealing spatially contiguous regions of residues linked to particular aspects of function. Regions included active-site proximal residues but extended to the enzyme surface, providing a map of underlying architecture not possible to derive from existing approaches. HT-MEK has applications that range from understanding molecular mechanisms to medicine, engineering, and design.

Understanding how sequence encodes function remains a fundamental challenge in biology. Linear chains of amino acids fold into three-dimensional protein structures that carry out the physical and chemical tasks needed for life, such as highly efficient and specific catalysis. Sequence variations across organisms and individuals confer beneficial and deleterious effects: Variation throughout evolution creates proteins with improved or new functions, but variation among individuals can also compromise function and cause disease (*1*–*3*). An enhanced predictive understanding of the sequence-function landscape could have profound impacts across biology, from enabling efficient protein design to improving detection of rare allelic variants that drive disease (*4*–*7*), but new approaches and data are needed to attain this goal.

Understanding sequence-function relationships within enzymes poses a particular challenge. Structural and biochemical studies of enzymes have revealed the sites of substrate binding and catalytic transformation, the residues directly involved in catalysis, and roles for these residues. Nevertheless, residues outside the active site are needed for the active site to assemble and function and for control of function by allosteric ligands and covalent modifications (*8*–*10*). Despite their importance, the roles played by residues outside the active site, which comprise the majority of amino acids in an enzyme, remain largely unexplored.

This dearth of knowledge stems from the nature of experimental approaches currently available. Site-directed mutagenesis (SDM) has traditionally been used to assess function by means of in-depth biochemical assays that yield kinetic and thermodynamic constants. However, SDM is time-, resource-, and labor-intensive, limiting investigation to a small number of residues. By contrast, deep mutational scanning (DMS) provides the ability to assay the effects of all 20 amino acids at every position within an enzyme (*5*, *11*, *12*). However, DMS lacks the depth and dimensionality of traditional SDM studies, typically providing a scalar readout with an uncertain relationship to the multiple fundamental physical constants needed to describe an enzyme's function.

Marrying the strengths of traditional SDM and emerging DMS is needed to usher in a new era of mechanistic enzymology. Here, we present HT-MEK (High-Throughput Microfluidic Enzyme Kinetics), a platform capable of simultaneously expressing, purifying, and characterizing more than 1500 rationally chosen enzyme mutants in parallel with the depth and precision of traditional SDM. Each HT-MEK experiment provides 1000s of measurements and multiple kinetic and thermodynamic constants [such as the apparent unimolecular rate constant (k_{cat}), Michaelis constant (K_m), k_{cat}/K_m, and inhibition constant (K_i)] in days and at low cost.

To guide HT-MEK development and demonstrate its capabilities, we carried out a comprehensive mechanistic investigation of the effects of mutations to every residue within the alkaline phosphatase superfamily member PafA (phosphate-irrepressible alkaline phosphatase of Flavobacterium) (Fig. 1A and fig. S1). PafA and related phosphomonoesterases are among the most prodigious catalysts known, with rate enhancements of up to ~10^{27}-fold, providing a large dynamic range to explore (*13*). We also anticipated that PafA, a secreted enzyme, would be highly stable, potentially allowing us to more deeply probe catalysis without obfuscation from global unfolding. We found that 702 of the 1036 mutants investigated have substantial functional consequences, with none arising from equilibrium unfolding. Additional experiments revealed that many mutations promote the formation of a long-lived, catalytically incompetent misfolded state both in vitro and in cells. The multidimensional measurements provided by HT-MEK allowed us to decouple this misfolding from catalytic effects and quantify mutational effects on particular aspects of catalysis and mechanism using an approach we call Functional Component Analysis. This approach revealed spatially contiguous regions of residues that extend from the active site to the enzyme surface responsible for optimizing particular catalytic strategies. Surface residues with functional effects upon mutation may compose candidate allosteric regions useful for engineering rational control of catalytic activity. The HT-MEK platform and the quantitative multidimensional datasets it can provide will have broad utility for future efforts to understand catalytic mechanisms, natural variation, and evolutionary trajectories and to design enzymes with new functions.

Results

HT-MEK device and experimental pipeline

HT-MEK is built around a two-layer polydimethylsiloxane (PDMS) microfluidic device with 1568 chambers and integrated pneumatic valves (Fig. 1B and fig. S2) (*14*, *15*). Each chamber is composed of two compartments (DNA and Reaction) separated by a valve (Neck), with adjacent chambers isolated from one another by a second valve (Sandwich). A third valve (Button) reversibly excludes or exposes a circular patch of the reaction compartment surface, enabling surface patterning for on-chip protein immobilization and purification (Fig. 1C) and subsequent simultaneous initiation of successive on-chip reactions across the device (Fig. 1D). Each DNA compartment of each chamber is programmed with a specified enzyme variant by aligning the device to a spotted array of DNA plasmids that encode for the expression of C-terminally enhanced green

[1]Department of Biochemistry, Stanford University, Stanford, CA 94305, USA. [2]Department of Bioengineering and Therapeutic Sciences, University of California, San Francisco, CA 94158, USA. [3]Department of Bioengineering, Stanford University, Stanford, CA 94305, USA. [4]Department of Biomedical Data Science, Stanford University, Stanford, CA 94305, USA. [5]Department of Statistics, Stanford University, Stanford, CA 94305, USA. [6]Department of Chemical Engineering, Stanford University, Stanford, CA 94305, USA. [7]ChEM-H Institute, Stanford University, Stanford, CA 94305, USA. [8]Department of Genetics, Stanford University, Stanford, CA 94305, USA. [9]Chan Zuckerberg Biohub; San Francisco, CA 94110, USA.
*Corresponding author. Email: herschla@stanford.edu (D.H.); pfordyce@stanford.edu (P.M.F.)
†These authors contributed equally to this work.

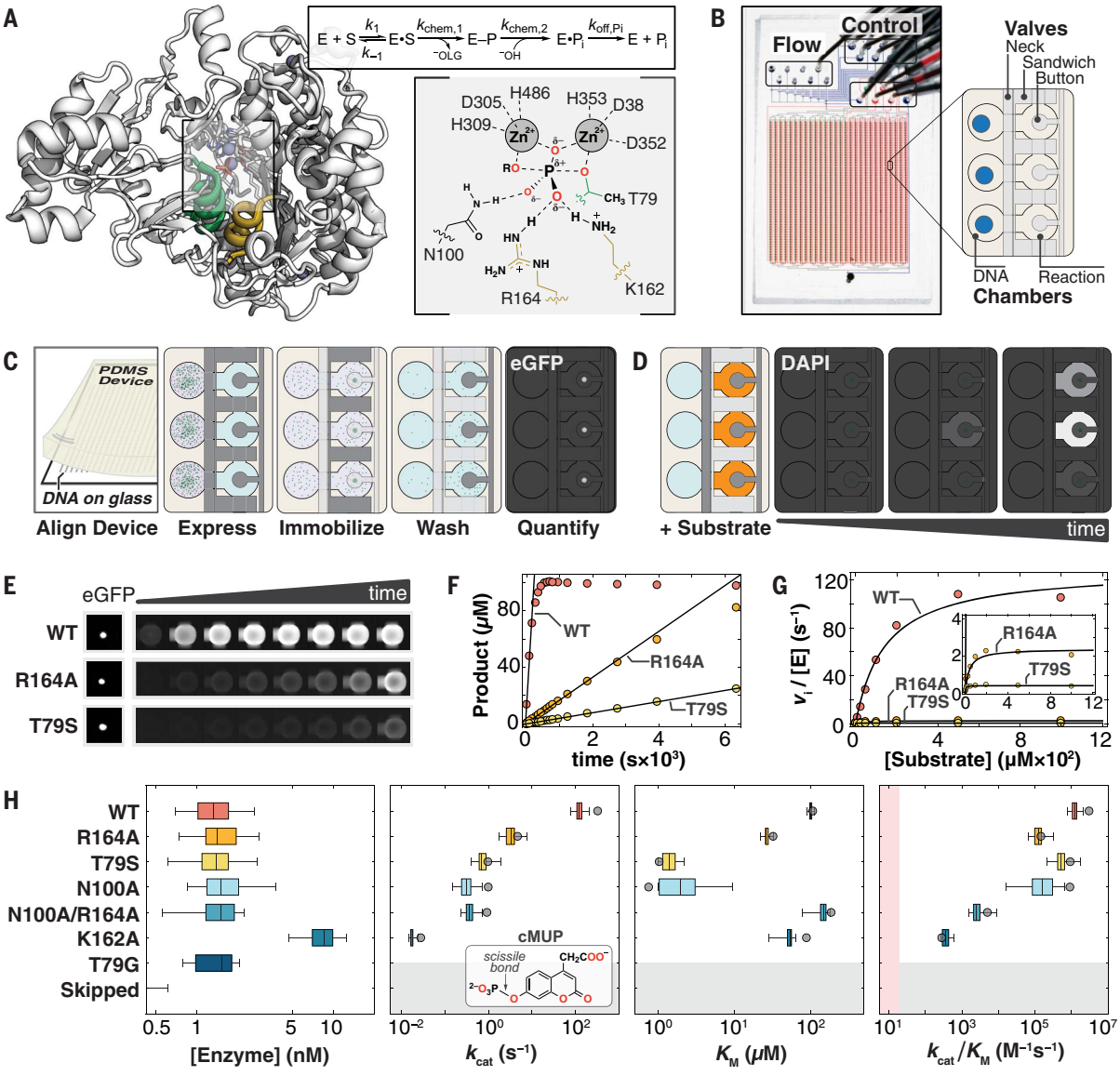

Fig. 1. Overview of HT-MEK and PafA. (**A**) (Left) Crystal structure of WT PafA [Protein Data Bank (PDB) ID: 5TJ3] highlighting "nucleophile" (residues 77 to 89, green) and "monoesterase" (residues 161 to 171, yellow) helices. (Right) PafA catalytic cycle (S, phosphate monoester substrate; E–P, covalent phospho-threonine intermediate; $^{-}$OLG, alkoxide leaving group) and active site in the transition state of monoester hydrolysis. (Single-letter abbreviations for the amino acid residues are as follows: A, Ala; C, Cys; D, Asp; E, Glu; F, Phe; G, Gly; H, His; I, Ile; K, Lys; L, Leu; M, Met; N, Asn; P, Pro; Q, Gln; R, Arg; S, Ser; T, Thr; V, Val; W, Trp; and Y, Tyr. In the mutants, other amino acids were substituted at certain locations; for example, T79S indicates that threonine at position 79 was replaced by serine.) (**B**) HT-MEK microfluidic device image and schematic showing solution (Flow) and pneumatic manifold (Control) input ports, device valves, and chambers. (**C**) Schematic of on-chip enzyme expression pipeline. Dark and light gray valves are pressurized (closed) and depressurized (open), respectively. (**D**) Schematic of on-chip activity assays by using fluorogenic substrate in reaction chambers (orange). (**E**) Sample images of (left) immobilized enzyme and (right) fluorogenic product over time for WT PafA and two active-site mutants (R164A and T79S) with the substrate cMUP. (**F**) Example cMUP progress curves for chambers containing wild type and two active-site mutants and initial rate fits to these data. (**G**) Michaelis-Menten fits to initial rates yield k_{cat}, K_m, and k_{cat}/K_m for cMUP. (**H**) (Left) On-chip expressed concentrations for WT PafA and six active-site mutants calculated by using eGFP calibration curves. (Middle left to right) Comparisons of on-chip (box plots) and off-chip (gray circle) values of k_{cat}, K_m, and k_{cat}/K_m values ($\log_{10}$ axis) for cMUP for seven PafA variants (table S1) and (inset) cMUP structure. K162A was expressed at higher concentration in a later experimental tier (with higher [E]); "skipped" refers to chambers without plasmid DNA; pink shaded region denotes 10-fold above the median apparent second-order rate constant for T79G control chambers (supplementary materials, materials and methods).

fluorescent protein (eGFP)–tagged variants (fig. S3). After alignment, device surfaces are patterned with antibodies to eGFP beneath the Button valve and passivated with bovine serum albumin elsewhere. All enzymes are then expressed in parallel through the introduction of an *Escherichia coli* in vitro transcription-translation system and purified by means of capture with surface-patterned immobilized antibody and washing (fig. S4). Production of up to 1568 different purified enzymes takes ~10 hours, with most steps automated. Enzymes are immobilized under the Button valves that protect against flow-induced loss of enzyme during solution exchange and allow repeated synchronous initiation of reactions.

To obtain catalytic rate parameters, we quantify (i) the concentration of immobilized

enzyme in each chamber, using an eGFP calibration curve (fig. S5), and (ii) the amount of product formed as a function of reaction time, using a chamber-specific product calibration curve (fig. S6). We then fit reaction progress curves in each chamber to obtain initial rates (v_i) for each substrate concentration using a custom image-processing pipeline and convert observed rates (v_i) to enzyme-normalized rate constants according to the eGFP intensity in each chamber and calibration curve (Fig. 1, E and F, and figs. S7 and S8). This process—repeated on a single device for multiple substrate concentrations, multiple substrates, and multiple inhibitors—provides the data necessary to obtain Michaelis-Menten parameters and other kinetic and thermodynamic constants (Fig. 1G and fig. S7).

HT-MEK reproduces kinetic constants previously measured with traditional assays

To demonstrate the technical capabilities of HT-MEK, we applied it to study seven previously characterized PafA variants: wild type, five active site mutants (T79S, N100A, R164A, K162A, and N100A/R164A), and one mutant lacking detectable activity (T79G, negative control) (*16*). Activities of wild-type (WT) PafA and the six mutants span a broad range in k_{cat} (>10^4-fold), k_{cat}/K_m (>10^4-fold), and K_m (>10^2-fold) for aryl phosphate monoester hydrolysis, providing a stringent initial test of HT-MEK dynamic range (table S1). Nearly all DNA-containing chambers expressed enzyme (>90%), and all mutants expressed at similar levels as determined from eGFP fluorescence (K162A was deliberately expressed at higher concentrations in a later experimental tier, described below) (Fig. 1H and fig. S9).

Although fluorogenic phosphate ester substrates permit kinetic assays of phosphatase activity with a high dynamic range, microfluidic assays that use the commercial 4-methylumbelliferyl phosphate ester (MUP) were complicated by partitioning of the hydrophobic fluorescent product into the hydrophobic PDMS, which increases background and distorts kinetic measurements. To address this limitation, we synthesized MUP derivatives of similar reactivity (cMUP and a corresponding methyl phosphodiester, MecMUP) that bear a charged moiety on the leaving group to eliminate PDMS absorption (figs. S10 to S12 and table S1).

Accurately resolving enzymatic rates spanning many orders of magnitude poses technical challenges because different acquisition times are needed at catalytic extremes (fig. S13), and even a small concentration of contaminating fast enzyme introduced into nearby chambers during fluid exchanges can obscure the true rates for the most catalytically compromised mutants. To address the first challenge, we expressed enzymes at two concentrations: ~1.5 nM (for accurate measurement of fast enzymes) and ~15 nM (to speed reactions for efficient detection of slow enzymes) (Fig. 1H and fig. S14). To identify regions of the device with contaminating enzymes from other chambers, we interspersed chambers that were empty or contained the inactive T79G mutant and also measured their apparent activity (figs. S15 and S16 and table S2). Per-device normalizations (0.4 and 1.4-fold) were used to account for small variations in apparent activity owing to nonspecific adsorption of mutant enzymes to chamber walls (supplementary materials, materials and methods). This normalization increased precision across replicates but did not affect conclusions (fig. S17). HT-MEK assays recapitulated cMUP kinetic parameters (k_{cat}, K_m, and k_{cat}/K_m) accurately and over a wide dynamic range (>10^4-fold in k_{cat}/K_m), indicating that the device and added eGFP tag did not alter activity (Fig. 1H and table S3).

Many mutations throughout PafA affect phosphate monoester hydrolysis

To explore functional effects of mutations throughout PafA, we created mutant libraries in which we introduced two residues with widely differing side-chain properties at each position: (i) glycine, to ablate side chain interactions and increase backbone flexibility, and (ii) valine, to introduce a branched chain hydrophobe of average volume. Native valine and glycine residues were mutated to alanine. Nearly all of these 1052 possible mutants (1036; 98%) were successfully cloned, sequenced, expressed, and assayed with HT-MEK (fig. S18).

We first measured the catalytic effect of each substitution on the steady-state kinetic parameters for cMUP hydrolysis (k_{cat}, K_m, and k_{cat}/K_m) (Fig. 2A). To facilitate efficient measurement, we performed experiments in three tiers based on reaction rates (table S2). In tier 1, we assayed devices that contained all variants at low enzyme concentration ([E] ~ 1.5 nM), with enzymes printed in duplicate and the above-noted active site mutants distributed throughout as fiducial controls. Tier 2 and 3 measurements, using higher enzyme concentration ([E] ≈ 15 nM), focused successively on the slowest variants with increasing assay times and increasing numbers of replicates to provide high-precision measurements of these slower mutants. Each device was used to measure tens of cMUP progress curves, and all expressed variants were stable over days, facilitating high-throughput data collection. Per-experiment data reports contain all data collected for each chamber, including initial rate plots and fit Michaelis-Menten curves (an example is provided in fig. S19, and full data sets are available as data files S1 and S2); per-mutant summaries combine data from all experiments and include estimates of statistical significance (Fig. 2, B and C, and fig. S20). In total, we acquired a median of nine and seven replicates for valine and glycine mutants, respectively, over 16 experiments (figs. S21 to 24 and table S2). The wealth and precision of these data allowed us to resolve differences across ranges of 10^4, 10^2, and 10^5-fold for k_{cat}, K_m, and k_{cat}/K_m, respectively.

As expected, mutations of active-site residues and catalytic Zn^{2+} ligands were highly deleterious, and positional effects varied for valine and glycine (Fig. 2, D to F). Nevertheless, a surprisingly large number of mutations throughout the enzyme were deleterious, with decreases in k_{cat}/K_m observed for 267 of the 1036 mutants ($P < 0.01$). We also observed 35 mutants with increased activity (fig. S21). These measurements provide a quantitative survey of Michaelis-Menten kinetic constants for mutations throughout a large enzyme but do not tell us why so many mutations alter activity.

The most obvious explanation for these widespread effects would be destabilization leading to a significant fraction of unfolded enzyme. Beyond destabilization, mutations can have other repercussions, altering the catalytic effectiveness of particular active-site residues, reducing Zn^{2+} affinity at the bimetallo active site or altering enzymatic protonation states. The ability to efficiently measure catalytic activity for all mutants under different assay and expression conditions as afforded by HT-MEK allowed us to test each of these possibilities.

Widespread mutational effects do not arise from equilibrium unfolding

Reflecting its role as a secreted phosphatase designed to function in harsh and variable environments, WT PafA is highly stable and remains folded, as inferred from circular dichroism (CD) spectra, even after exposure to 4 M urea for 14 days (fig. S25). This stability suggests that any individual mutation is unlikely to substantially unfold the enzyme. To directly test this expectation, we measured cMUP activities in the presence of increasing concentrations of urea. If a variant were already partially unfolded in the absence of urea, then even low concentrations of added urea would cause substantial additional unfolding (*17*), proportionally lowering activity (Fig. 2G and supplementary text S1). By contrast, we observed only minor rate effects for all mutants (six ± onefold decrease at 3 M compared with 0 M urea, ±SEM), which is considerably less than the >10^9-fold decrease predicted for an unfolding effect and consistent with inhibition by urea, with K_i = 2.6 M for all variants (Fig. 2H and fig. S26).

Equilibrium unfolding would also predict a Zn^{2+} concentration dependence for the observed rate because added or removed Zn^{2+} would pull the equilibrium between folded (and Zn^{2+}-bound) and unfolded states (Fig. 2G). Consistent with an absence of unfolding

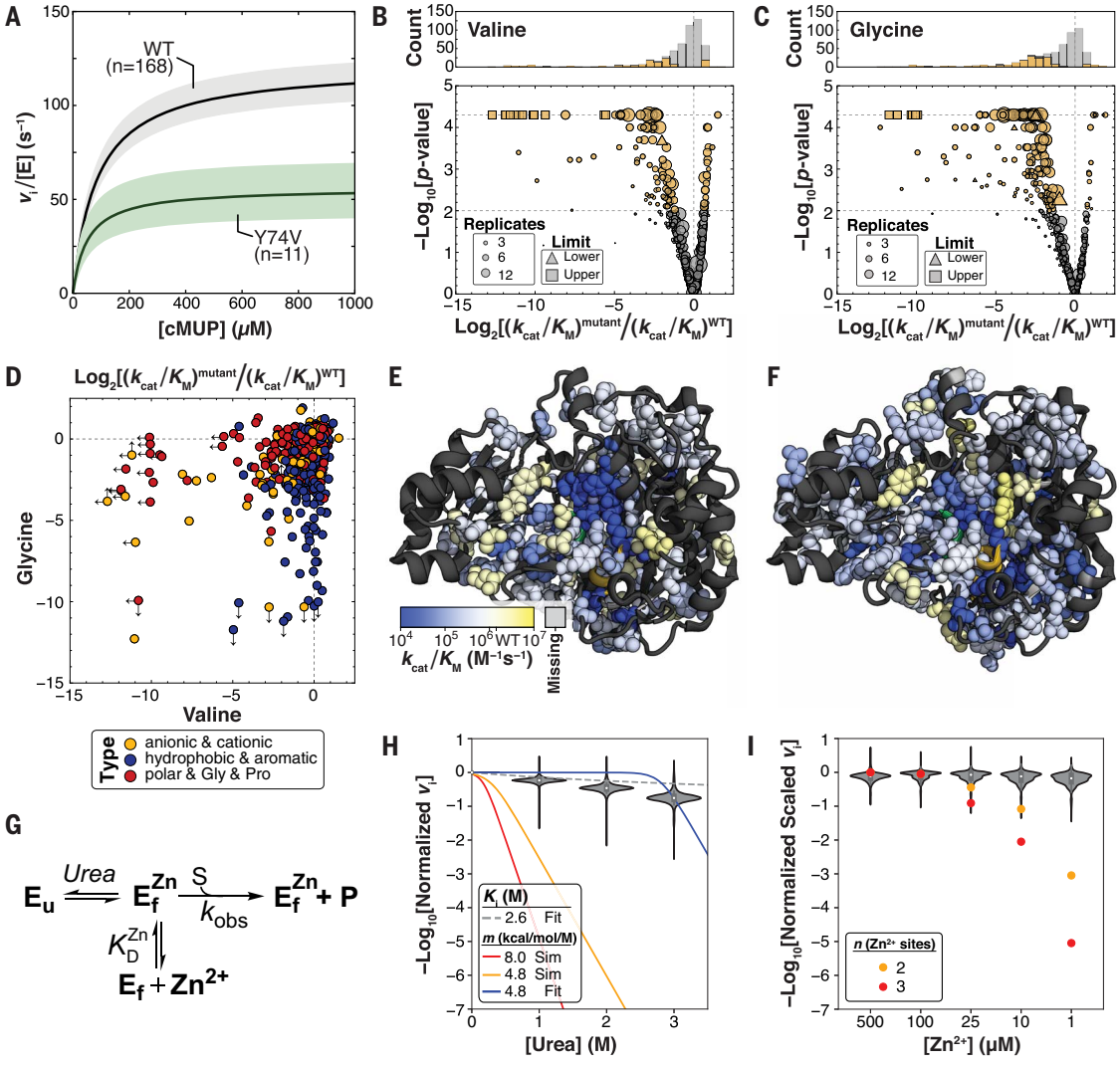

Fig. 2. HT-MEK measurements of aryl phosphate monoester (cMUP) hydrolysis for valine and glycine scans of PafA. (**A**) Median Michaelis-Menten curves for WT PafA and an example mutant with k_{cat} and K_m effects. Colored regions denote 99% confidence intervals (CIs) on medians of parameters from replicates. (**B**) Valine substitutions at 126 positions alter cMUP k_{cat}/K_m at $P < 0.01$ (105 slower, 21 faster, gold markers; gray, $P \geq 0.01$). (**C**) Glycine substitutions at 176 positions alter cMUP k_{cat}/K_m at $P < 0.01$ (162 slower, 14 faster, gold; gray, $P \geq 0.01$). (**D**) Effect of glycine versus valine substitution on cMUP k_{cat}/K_m at each position, colored by identity type of the native residue. Arrows denote the presence and direction of measurement limits. (**E** and **F**) Valine (E) and glycine (F) substitution effects on cMUP hydrolysis on the PafA structure. $P < 0.01$ sites shown as spheres, $P \geq 0.01$ and missing sites shown as ribbons. Alternate views are provided in fig. S21. (**G**) Model of equilibrium unfolding with varying urea and Zn^{2+}. (**H**) Activity of mutants relative to wild type at 50 μM cMUP as a function of urea. Red and yellow lines show predicted dependencies if mutants were 10% unfolded in the absence of urea, assuming *m* values of 4.8 and 8 kcal/mol/M (supplementary text S1). The blue curve is the best fit of the data for $m = 4.8$ kcal/mol/M with fraction unfolded (f_u) at 0 M [urea] as a free parameter (fit $f_u = 1 \times 10^{-10}$), and the dashed gray curve is the fit competitive inhibition of WT PafA by urea (fig. S26). (**I**) Normalized activity of mutants relative to wild type as a function of [Zn^{2+}]. Orange and red points show expected activities for Zn^{2+}-dependent unfolding events if mutants were 10% unfolded at 100 μM Zn^{2+} assuming two or three Zn^{2+} binding events, respectively.

effects, we observed no dependence on Zn^{2+} concentration over a ~10^3-fold range (Fig. 2I and supplementary text S1). This observation also establishes that observed rate effects for mutants with measurable rates do not arise from loss of bound Zn^{2+} owing to lowered Zn^{2+} affinity. Last, mutants were unaltered in their pH dependencies (fig. S27 and supplementary text S1), ruling out altered protonation states as responsible for observed kinetic effects.

A general high-throughput assay for phosphate release and additional mutational effects

Although fluorogenic probes provide a sensitive and convenient method for directly visualizing enzyme activity in kinetic assays, many reactions lack a direct fluorogenic readout. To allow future application of HT-MEK to a much broader range of enzymes, we developed an on-chip coupled assay in which inorganic phosphate (P_i) is detected through fluorescence emitted upon binding to a modified phosphate binding protein (PBP) (Fig. 3A) (*18*). Calibration curves for P_i and PBP and control measurements using the PafA substrate methyl phosphate (MeP) established that this coupled on-chip assay can detect submicromolar P_i formation and accurately reproduce off-chip kinetic constants (figs. S28 to S30).

Beyond their limited availability, fluorogenic substrates are often more reactive than

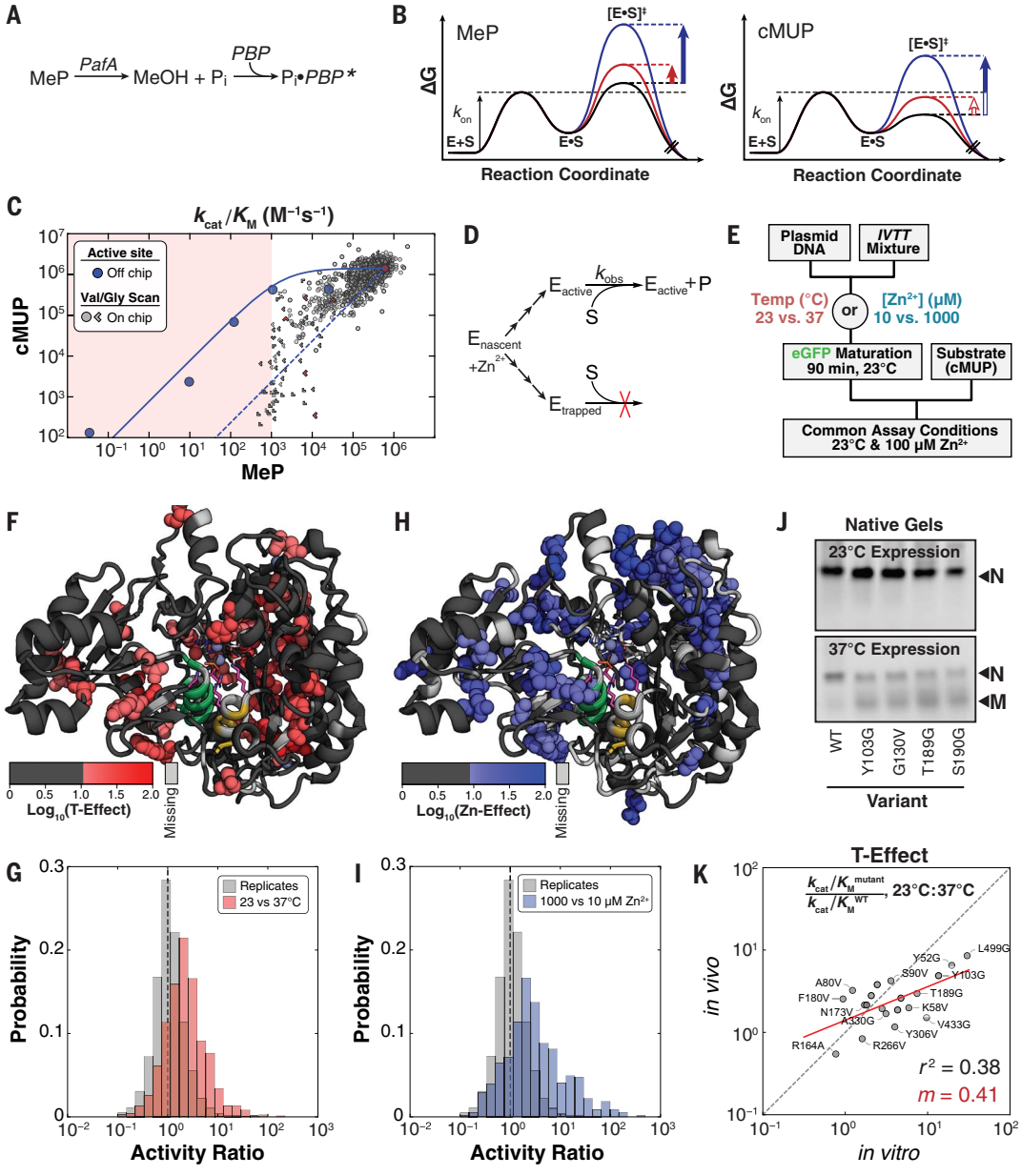

Fig. 3. Substrates with different intrinsic reactivity reveal kinetic folding traps. (**A**) Schematic illustrating real-time detection of P_i produced by MeP hydrolysis on-chip using a fluorophore-conjugated PBP (*18*). (**B**) Reaction coordinate diagrams schematically illustrating substrates with either chemistry (MeP) or binding (cMUP) as the rate-limiting step. Solid arrows indicate observable mutational effects on the chemical step, and open arrows indicate effects that are not observable. (**C**) Measured k_{cat}/K_m for MeP versus k_{cat}/K_m for cMUP for active-site mutants off-chip (blue points) and for valine and glycine mutants. Limits in one or both directions are indicated with chevrons pointing in the direction or quadrant of the limit. The red shaded region denotes lower limit of detection for MeP, the solid blue line indicates predicted relationship between k_{cat}/K_m for cMUP and MeP hydrolysis, and the dashed blue line shows predicted relationship for enzymes with WT activity but a varying fraction of inactive enzyme (supplementary text S2). (**D**) Scheme showing kinetic partitioning between folded (active) and misfolded (kinetically trapped) enzyme during expression. (**E**) Pulse-chase experiment to test for expression-dependent misfolding by varying expression conditions while keeping reaction conditions constant. (**F**) Residues with temperature-dependent activity changes shown as spheres on the PafA structure, with active-site residues N100, K162, R164, and T79 shown as purple sticks. (**G**) Histograms of the ratio of measured activities after expression at 23° and 37°C [cMUP (k_{cat}/K_m^{mutant})/(k_{cat}/K_m^{WT}), 23°C/37°C] (red) compared with the ratios of randomly paired replicates expressed under standard conditions (37°C and 100 μM Zn^{2+}; gray). (**H**) Residues with expression [Zn^{2+}]–dependent activity changes shown as spheres on the PafA structure. (**I**) Histograms of the ratio of measured activities across Zn^{2+} concentrations [cMUP (k_{cat}/K_M^{mutant})/(k_{cat}/K_M^{WT}), 1000 μM/10 μM Zn^{2+}] (blue) compared with the ratios of randomly paired replicates expressed under standard conditions (37°C and 100 μM Zn^{2+}; gray). (**J**) (Top) Native gels for enzymes expressed by means of in vitro transcription-translation off-chip at 23°C. All constructs appear as a single band corresponding to the natively folded species ("N"). (Bottom) At 37°C, non-WT variants have an additional band corresponding to the putatively misfolded ("M") species. (**K**) Expression temperature effects on-chip (in vitro) versus in *E. coli* (in vivo). The red line indicates linear regression of log-transformed data with the indicated slope (values provided in table S5). In vivo protein levels were determined from eGFP fluorescence to estimate total expressed protein concentration.

naturally occurring substrates, potentially rendering binding rate–limiting and obscuring mutational effects on the chemical step of catalysis, and there is evidence for this behavior with PafA (*16*). On-chip MeP hydrolysis assays, therefore, complement the wide dynamic range of cMUP assays by identifying modest effects on the chemical step. Off-chip measurements of several active-site mutants revealed a decrease in observed MeP activity (owing to effects on the chemical step) without a concomitant change in cMUP activity, as expected for rate-limiting cMUP binding (Fig. 3B, red vertical arrows). Once transition-state destabilization was sufficiently large, MeP and cMUP reactions both slowed (Fig. 3B, blue vertical arrows). The solid blue line in Fig. 3C is a fit to the rate model derived from the free energy–reaction profiles in Fig. 3B for a series of active-site mutants (Fig. 3C, blue points; figs. S31; and supplementary text S2) (*19*) and predicts the kinetic behavior expected for the PafA glycine- and valine-scanning library mutants.

HT-MEK kinetic measurements revealed k_{cat}/K_m effects for almost half of the mutants (498 of 1035 with $P < 0.01$) (fig. S32), but few exhibited the predicted behavior (Fig. 3C, solid blue line versus gray symbols). Instead, the mutants tended to fall between the predicted line and a diagonal line representing equally deleterious effects on the reactions of both substrates (Fig. 3C, blue solid and dashed lines, respectively). Equally deleterious effects are expected for enzymes with WT activity but only a fraction of the enzyme in the active configuration, with less correctly folded variants further down the diagonal. Thus, observed intermediate effects could represent combinations of effects on the chemical step and on the fraction of the mutant population that is active.

Many mutations reduce catalysis by altering folding

The urea, Zn^{2+}, and pH data presented above provided strong evidence against equilibrium unfolding for any of the variants (Fig. 2, H and I). We therefore considered and tested an alternate model in which inactive enzyme resulted from a nonequilibrium process: the formation of long-lived misfolded proteins during expression (Fig. 3D) (*20*). Because temperature is known to affect folding efficiency (*21*, *22*), and because PafA binds multiple Zn^{2+} ions during folding, we varied the expression temperature (23° and 37°C) and Zn^{2+} concentration (10 and 1000 μM) from our standard expression conditions (37°C and 100 μM Zn^{2+}). We then measured reaction rates under identical assay conditions (23°C and 100 μM Zn^{2+}, our standard assay conditions), so that any observed rate changes must arise from differences during folding that persisted over time (Fig. 3E). Many mutations had differential effects on observed catalytic activity when expressed at 23° versus 37°C ("T-Effect") or with different concentrations of Zn^{2+} ("Zn-Effect"). Whereas T-Effects were found predominantly in the enzyme core, Zn-Effects were concentrated around the distal Zn^{2+} (Fig. 3, F to I, and figs. S33 and S34). These results strongly support the presence of persistent nonequilibrium folding effects, which have been anecdotally observed in other systems (*20*, *21*, *23*–*25*). A second prediction of the misfolding model was also met: Variants with T- and Zn-Effects were not systematically altered in K_m under varied expression conditions (fig. S35), as expected under a model of nonequilibrating states. PafA folding thus apparently involves one or more branchpoints sensitive to temperature and Zn^{2+} that lead to active PafA or one or more long-lived inactive states (Fig. 3D).

Altered folding pathways promote a long-lived inactive state in vitro and in vivo

Misfolding could be an artifact of high-throughput on-chip expression or could also arise during standard expression in vitro and possibly in vivo. To test for chip-induced misfolding effects, we selected 19 variants with varying predicted amounts of misfolding for off-chip expression by means of in vitro transcription-translation and kinetic characterization (fig. S36 and table S4). Activities were similar off- and on-chip (fig. S37), suggesting that the chip is not responsible for the observed misfolding.

Native gels and kinetic assays provided additional support for the misfolded state. Mutants predicted to misfold had an additional band of distinct mobility when expressed at high temperature that was not present or diminished when expressed at lower temperature (Fig. 3J, misfolded state "M"). Transient treatment with thermolysin, a protease that cleaves within exposed hydrophobic regions that occur in unfolded or misfolded proteins, resulted in loss of M but not the native state (native state "N") (fig. S38A) (*26*). Nevertheless, despite degradation of the majority of the protein (present as M), the total observed enzyme activity for each mutant was unchanged before and after degradation (fig. S38B), indicating that M lacked substantial activity and that N and M did not equilibrate over the hours taken to carry out these experiments. The observation that different temperature-sensitive mutants gave the same mobility on a native gel and similar protease sensitivity suggests the formation of a single misfolded state or set of states with similar properties.

Our observation of a long-lived inactive state raised the question of whether analogous misfolding occurs in cells, where cellular machinery can assist folding. We recombinantly expressed 21 variants in *E. coli* that did and did not undergo temperature-dependent misfolding in vitro (fig. S36 and table S5). Expression in vivo was also temperature dependent, with changes in apparent k_{cat}/K_m values for the in vivo–expressed PafA mutants that correlated with the change observed in vitro [coefficient of determination (R^2) = 0.38] (Fig. 3K). Temperature effects were generally smaller for in vivo–expressed mutants, suggesting that cellular factors may partially rescue or preferentially degrade the misfolded state, analogous to cellular degradation of thermodynamically destabilized mutants (*27*).

To test whether misfolding was a consequence of the eGFP tag, we overexpressed a non–eGFP-tagged variant (Y103G). We found wild type–like activity when it was expressed at 23°C but 260-fold less activity when it was expressed at 37°C (table S6 and fig. S39), suggesting that >99% of the 37°C-expressed enzyme was in the M state. CD spectra of the purified Y103G mutant provided independent evidence for a structural alteration that accompanied misfolding in vivo. WT PafA exhibits identical CD spectra when expressed at 37° or 23°C; by contrast, the CD spectrum for Y103G matches that of wild type when the mutant is expressed at low temperature (23°C) but not at higher temperature (37°C) (fig. S40), with the observed difference at 37°C suggesting loss of about one-third of PafA's α-helical character in M (table S7).

Together, these results suggest that cellular folding conditions and chaperones are insufficient to prevent mutations from causing PafA to misfold and form long-lived inactive states in an *E. coli* expression strain [BL21 (DE3)]. However, the degree to which misfolding is rescued likely varies between strains and is sensitive to growth conditions and expression levels (*28*). A tendency to form kinetically stable misfolded states may therefore exert a selective pressure and influence the fitness landscape of proteins in cells (*29*–*33*).

Dissecting the origins of observed catalytic effects

HT-MEK assays allow us to quantify and dissect the degree to which observed changes in activity arise from changes in the amount of expressed protein, the amount that is correctly folded, and the catalytic efficiency of the correctly folded enzyme. Below, we isolate the catalytic effects for our PafA variants. We then take advantage of HT-MEK's ability to provide quantitative kinetic and thermodynamic constants for multiple substrates and inhibitors and use these data to probe PafA's functional architecture at a global level.

To remove folding effects, we compared k_{cat}/K_m values measured for substrates with different rate-limiting steps (cMUP and MeP) (Fig. 3C and supplementary text S3 and S4), represented the datapoint for each PafA variant in Fig. 3C as a superposition of a catalytic

effect (Fig. 3C, blue solid line, defined by PafA active site variants that do not have misfolding effects; fig. S41) and a misfolding effect (Fig. 3C, diagonal blue dashed line), and solved for both (Fig. 4A and fig. S42). With this approach, we were able to quantify catalytic effects (k_{cat}/K_m^{chem}) for 946 of the 1036 variants and obtain upper limits for an additional 65 (fig. S43). Deleterious catalytic effects were found for mutations at 161 of PafA's 526 positions (Fig. 4B, figs. S44 and S45, and table S8). Mutations at an even larger number of positions, 232, gave folding effects. The magnitude of folding effects did not correlate with observed eGFP fluorescence intensities, establishing that enzyme misfolding does not influence eGFP folding (fig. S46).

The largest catalytic effects cluster in and around the active site, with the fraction of residues exhibiting effects diminishing with distance from the active site (Fig. 4C and table S8). Although positions that give catalytic effects tend to cluster, the pattern is asymmetric and complex (Fig. 4D). Many large distal effects are found surrounding the bound Zn^{2+} that is >15 Å from the active site ("distal Zn^{2+}"), suggesting that its coordination may restrain the conformational mobility of surrounding residues and propagate to the active site. Nevertheless, it is difficult to rationalize catalytic effects, especially more distal effects. To better understand these patterns and to relate effects to the specific mechanisms used in catalysis, we defined functional components (FCs) from prior mechanistic studies of PafA and other alkaline phosphatase (AP) superfamily members (*16*, *34*, *35*) and systematically assessed the effect of each mutation on each FC.

FC1: Mutations disrupting O2 phosphoryl oxygen atom interactions

Our first FC (FC1) is derived from the observation that removal of two active-site side chains, K162 and R164, reduces monoester hydrolysis by 10^5-fold but has no effect on diester hydrolysis, rendering PafA an equally potent phosphate mono- and diesterase (fig. S47) (*16*). Because K162 and R164 interact with the phosphoryl oxygen that is anionic in monoesters but esterified in diesters (Fig. 5A, O2) (*34*), we expect other residues that support the formation of these interactions to similarly disrupt monoester but not diester hydrolysis. We define these effects as FC1 = $\Delta^{diester}/\Delta^{monoester}$, where $\Delta = (k_{cat}/K_m)^{mutant}/(k_{cat}/K_m)^{WT}$. Although the simplest expectation is that mutations to residues neighboring K162 and R164 will have FC1 effects, we cannot predict how large and how varied these effects are, how far they extend, or whether there are remote regions or surface sites that have large effects. In addition, we cannot predict whether residues that affect FC1 also contribute to other catalytic mechanisms, represented as other FCs below.

To measure diester activity on-chip and determine FC1 effects, we synthesized a fluorogenic diester substrate suitable for HT-MEK (MecMUP) and measured k_{cat}/K_m for the PafA mutant libraries (high K_m values for the noncognate diesterase activities preclude estimation of k_{cat} and K_m separately) (fig. S48) (*16*). We obtained k_{cat}/K_m values for 857 of the 1036 mutants and upper limits for an additional 178 (fig. S49, A and B), and on-chip diester rate constants matched off-chip measurements (fig. S49C). Because folding affects hydrolysis of both substrates equally, we compared measured rates directly, without correcting for folding effects (fig. S50A), allowing stronger statistical inference (fig. S50B).

Many mutants had FC1 effects: 88 Val and 93 Gly mutations (fig. S50C), corresponding to 156 of the 494 measurable positions (of a total of 526 positions) (Fig. 5, B to D). Seven of the 10 measurable non–active-site residues directly contacting K162 or R164 (second-shell residues) exhibited FC1 effects (Fig. 5E; fig. S51, A and B; and table S9A), which is consistent with frequent second-shell effects observed in directed evolution experiments (*36*–*38*). Of the three active-site Zn^{2+} ligands with measurable effects upon mutation, we observed an FC1 effect for D38G (which accepts a hydrogen bond from K162) but no FC1 effect for D352G or H353V (which do not interact with K162 or R164). The active-site variants T79S and N100G also had FC1 effects (tables S9B and S10), which is consistent with coupling between active-site residues attributable to shared contacts with K162 and R164 (Fig. 5E).

Although the largest effects were observed for active-site residues and next-largest for the second-shell residues, there was no additional drop in effect size after the third shell; the majority of residues with >10-fold FC1 effects were found in the third shell and beyond (15 of 23) (fig. S51 and table S11). Four of these lie at the enzyme surface (Fig. 5D and fig. S51), which is consistent with the hypothesis that

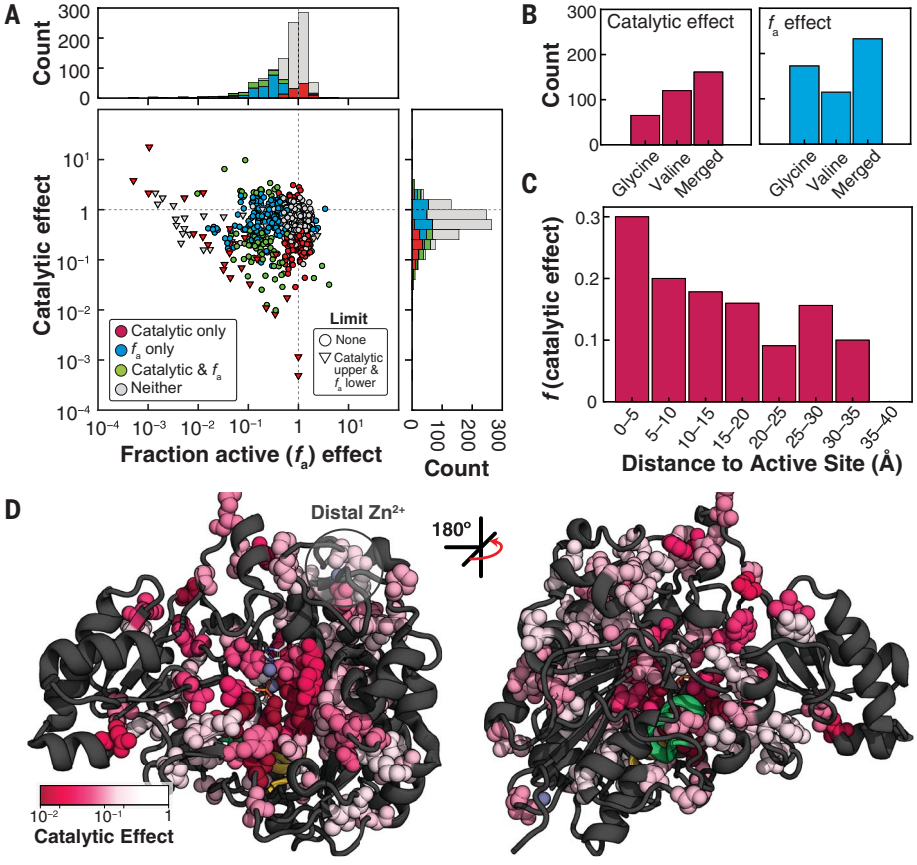

Fig. 4. Separating mutational effects on catalysis from changes in the fraction of active enzyme (f_a). (**A**) Catalytic and f_a effects (relative to wild type) for all variants colored by effect. Distributions of effects are projected along axes (stacked). (**B**) Counts of mutants with catalytic ($P < 0.05$) and f_a effects ($P < 0.01$) for the valine and glycine libraries, and total number of positions with effects (out of 525, "Merged") (fig. S45). (**C**) Fraction of non–active-site mutants within each distance bin with deleterious catalytic effects. $P < 0.05$; 5-Å bins (table S8). (**D**) Positions with deleterious catalytic effects on the PafA structure [161; "Merged" set in (B)]. Residues with deleterious effects (greater than fivefold down from wild type) are colored according to the most deleterious effect and shown as spheres.

enzymes possess a reservoir of allosteric potential and suggests that HT-MEK can be used to identify regions that are potential sites for allosteric inhibitors and drugs (*39*–*43*).

PafA has three of four nonterminal auxiliary domains (ADs) found within the AP superfamily, referred to as ADs 2 to 4 (supplementary text S5), that sit around the universally conserved Rossmann fold (Fig. 5F and fig. S52). ADs 2 and 4 are present in both AP superfamily phosphate mono- and diesterases, whereas AD 3 contains K162 and R164 and is considerably more extensive in the monoesterases (figs. S52 and S53 and table S12). Despite these apparent functional and evolutionary differences, FC1 effects are found in all three ADs to a similar extent and with similar magnitudes (fig. S54 and table S13). The largest FC1 effect outside of the active site or second shell comes from a solvent-exposed surface residue, D473, within AD 4 (Fig. 5F, yellow); a dramatically larger effect for the valine substitution (>60-fold versus less than twofold for D473G) suggests that a change in local folding may allosterically disrupt the O2 site 20 Å away. Two nearby residues (L434 and I451) also exhibit >10-fold FC1 effects, and all three lie along a three-way interface between ADs 3 and 4 and the Rossmann core domain (Fig. 5F). Future multimutant cycle experiments (*44*–*46*) using HT-MEK may allow testing of whether mutations at interfaces result in more extensive conformational rearrangements than mutations within a single domain and dissect the underlying structural properties accounting for long-range effects.

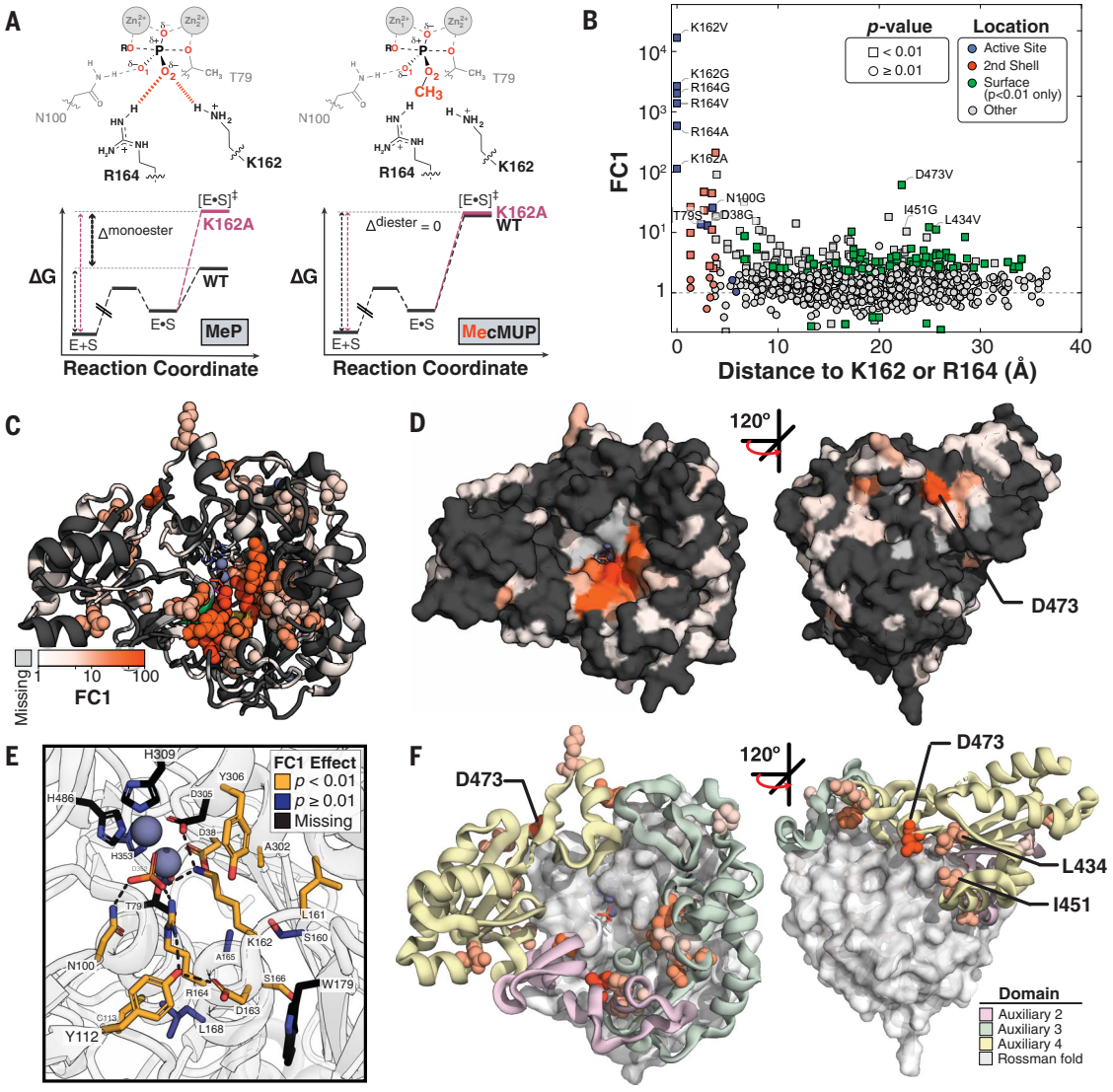

Fig. 5. FC1: Catalytic effects through the O_2 phosphoryl oxygen atom. (**A**) Schematic of the transition states for reaction of (left) MeP and (right) MecMUP highlighting the methyl group on the O_2 phosphoryl atom of MecMUP (orange) and the O_2 interactions with K162 and R164. Thin black and pink arrows indicate the reaction barrier for wild type and a mutant PafA, respectively, for each reaction; the thick black arrow denotes their difference for the two reactions ($\Delta^{monoester}$ and $\Delta^{diester}$). The ratio of k_{cat}/K_m effects (the difference between $\Delta^{monoester}$ and $\Delta^{diester}$ in energy space) gives FC1. (**B**) FC1 values as a function of the minimum distance to K162 or R164, with active site, second shell, and significantly affected surface residues colored. (**C**) PafA positions with FC1 effects ($P < 0.01$) when mutated to valine or glycine, colored by FC1 magnitude. Effects greater than fivefold are shown as spheres, with ribbon coloring for positions with effects less than or equal to fivefold. (**D**) PafA surface representation with FC1 effects colored as in (C). (**E**) FC1 effects of active site and second-shell residues indicating residues with significant FC1 effects (yellow), without FC1 effects (blue), and without measurements (black) (table S9). (**F**) Distribution of FC1 effects within the Rossmann core and Auxiliary Domains. Distal (greater than or equal to third shell) positions with effects greater than fivefold shown as spheres colored corresponding to their auxiliary domain. Only effects in auxiliary domains are shown.

FC2 and FC3: Effects on phosphate affinity

To provide catalysis, enzymes must bind their transition states more strongly than their substrates; otherwise, the energetic barrier for the reaction and reaction rate would remain the same as in solution (*47*, *48*). Enzymes must also limit the binding of substrates and products to allow sufficient turnover in the presence of higher substrate and product concentrations (*49*, *50*). Ground-state destabilization has been considered a possible mechanism for achieving this, and there is evidence for ground-state destabilization by PafA and other AP superfamily members through electrostatic repulsion between the anionic nucleophile, T79 in PafA, and the negatively charged phosphoryl oxygens (Fig. 6A) (*16*, *35*, *51*). For PafA, mutating T79 to serine increases the affinity for P_i, the reaction's product and a ground-state analog, by 100-fold, whereas in *E. coli* AP, the nucleophile S102G mutation increases affinity more than 1000-fold (*16*, *35*); the S102G mutation ablates the nucleophile entirely, and the chemically conservative T79S substitution presumably allows greater mobility, reducing electrostatic repulsion (*16*). We therefore expect that mutations that perturb this mechanism will increase P_i affinity and define the second FC, FC2, as strengthened P_i binding ($K_i^{mutant}/K_i^{WT} < 1$).

Conversely, active-site residues typically make both ground-state and transition-state interactions, so their removal weakens binding and diminishes catalysis, in some instances to a similar extent ("uniform binding") and in others preferentially destabilizing the transition state (*52*–*55*). As expected, mutations to the PafA active-site residues that interact with the phosphoryl O1 and O2 oxygen atoms (N100, K162, and R164) weaken P_i binding, but N100 and K162 mutations have much larger effects on catalysis, indicating preferential transition-state stabilization (fig. S55) (*16*). We therefore define the third FC (FC3) as weakened P_i binding ($K_i^{mutant}/K_i^{WT} > 1$).

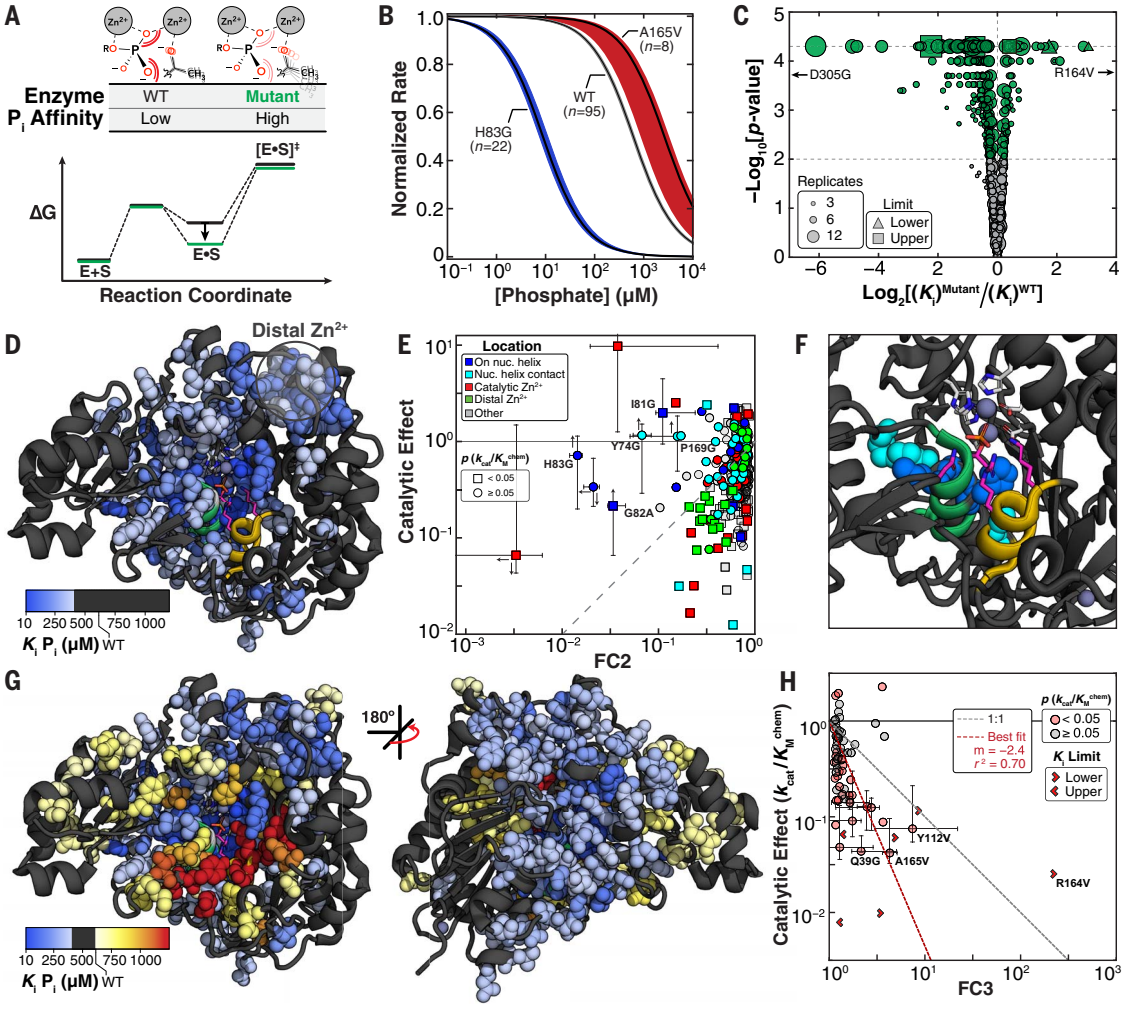

Fig. 6. FC2 and FC3: Mutational effects on affinity for P_i. (**A**) Reaction coordinate diagram for hypothetical mutant (green) with diminished destabilization relative to wild type (black) and schematic illustrating a model for an FC2 effect through increased flexibility of the T79 nucleophile. (**B**) Median P_i inhibition curves for wild type and two mutants with FC2 (H83G) and FC3 (A165V) effects. Colored regions denote 99% CIs on the medians of replicate measurements. (**C**) Volcano plot of K_i P_i effects for glycine and valine scan mutants. $P < 0.01$, green markers; $P \geq 0.01$, gray markers. (**D**) PafA structure with positions for which K_i P_i is >1.5-fold tighter than that of wild type (at $P < 0.01$) shown as spheres colored by the magnitude of the larger effect. The "nucleophile" helix (green) is largely obscured. (**E**) Scatter plot of catalytic and FC2 effects ($P < 0.01$) colored by location. Error bars correspond to 95% CIs determined from bootstrapping; up and down arrows indicate lower and upper k_{cat}/K_m^{chem} limits, respectively; left and right arrows indicate upper and lower K_i P_i limits. (**F**) PafA active-site (pink residues) and the five mutants possessing large FC2 effects without k_{cat}/K_m^{chem} effects shown as spheres, corresponding to the labeled mutants in (E). (**G**) Front and back views of FC2 (blue spheres) and FC3 effects (red spheres). FC2 effects are those shown in (D), and FC3 effects are shown for $P < 0.01$. (**H**) Scatter plot of catalytic (k_{cat}/K_m^{chem}) and FC3 effects for mutants with FC3 effects ($P < 0.01$). Gray and red points indicate significant and insignificant k_{cat}/K_m^{chem} effects, respectively. Error bars correspond to 95% CIs, as in (E); red dashed line indicates the best fit line to mutants with significant FC3 and catalytic (k_{cat}/K_m^{chem}) effects, excluding active-site mutants.

To measure inhibition constants, we quantified rates of cMUP hydrolysis as a function of P_i concentration and fit observed initial rates to a competitive inhibition model (Fig. 6B and fig. S56). HT-MEK–determined inhibition constants agreed with previous off-chip measurements (fig. S57) and are of higher precision than kinetic constants because they are not sensitive to uncertainties in total enzyme concentration or active fraction (Fig. 6C; reports of inhibition measurements are available in data files S1 and S2).

We uncovered 331 mutants that increased P_i affinity (FC2) and 73 that decreased P_i affinity (FC3) (Fig. 6C and fig. S58). Thus, about one-third of all mutants measurably altered affinity, and four times as many mutations enhanced binding as weakened it. Because it is highly unusual to enhance function through random variation, this observation suggests that residues at many positions are evolutionarily selected to prevent tight P_i binding. Mutations with ground-state destabilization effects (FC2) were located in an extended yet spatially contiguous region that included the helix containing the T79 oxyanion ("nucleophile helix"), the catalytic Zn^{2+} ions, and the distal Zn^{2+} site (Fig. 6D and tables S14 and S15).

Catalytic effects (k_{cat}/K_m^{chem}) for mutants with FC2 effects ranged from insignificant to 100-fold reductions (Fig. 6E and fig. S59). For most, the catalytic effect was greater than the FC2 effect, which is consistent with functional roles beyond the prevention of too-tight binding. Nevertheless, five mutants of residues that form a spatially contiguous subregion on and adjacent to the nucleophile helix have the largest FC2 effects but little or no catalytic effect (Fig. 6E and F), suggesting that these mutations allow rearrangements to reduce electrostatic repulsion in the presence of bound substrate.

Mutants that weakened P_i binding (FC3 effects) were also located in a contiguous region (Fig. 6G). The largest FC3 effects were near active-site residues K162 and R164 and had larger effects on catalysis (k_{cat}/K_m^{chem}) than P_i binding (Fig. 6H, red, and figs. S60 to S62), presumably reflecting the greater constraints present in the transition state than in the ground state (*56*, *57*).

Comparisons of the mutational effects across FC1 to FC3 reveal that many mutations outside the active site preferentially affect either FC1 or FC2. Further, several preferentially alter FC2 without dramatically altering FC1, reducing the fraction of active enzyme, or reducing overall catalysis (fig. S63). A small number of residues at the interface of FC2 and FC3 effects yield either an FC2 or FC3 effect depending on the substitution (fig. S64). The ability to selectively alter particular properties through specific mutations provides a potential starting point for attempts to engineer enzymes with desired kinetic and thermodynamic constants and behaviors.

FC4: Rates of phosphoenzyme hydrolysis

Linking observed mutational rate effects to their physical and chemical origins requires knowledge of the step that is being observed: the rate-limiting step. Pre–steady-state approaches (such as stopped flow and rapid quench) are the gold standard for determining rates of individual reaction steps but do not readily scale to large libraries. For PafA, extensive prior mechanistic knowledge allowed us to determine mutational effects on individual PafA reaction steps for 992 PafA variants without requiring pre–steady-state measurements.

The steady-state kinetic constant k_{cat}/K_m can be limited by substrate binding or chemical cleavage of the substrate to form the covalent enzyme-phosphate (E–P) species (Fig. 7A, k_1 and $k_{chem,1}$ steps), and k_{cat} can be limited by hydrolysis of E–P ($k_{chem,2}$) or dissociation of product P_i ($k_{off,Pi}$) (Fig. 7A). We deconvoluted mutational effects on $k_{chem,2}$ using measurements of k_{cat} for cMUP and K_i for P_i, and these $k_{chem,2}$ effects define FC4 (supplementary text S6). Seven mutants changed the rate-limiting step from E–P hydrolysis to P_i release ($k_{off,Pi} < k_{chem,2}$) (fig. S65), which is consistent with the observation of naturally occurring alkaline phosphatases of the AP superfamily with either of these steps rate limiting (*58*).

Overall, we found 18 Val and 36 Gly mutants that reduce $k_{chem,2}$ (Fig. 7B and fig. S66), and these overlap substantially with those affecting k_{cat}/K_m^{chem} (table S16). In the simplest scenario, mutations reducing $k_{chem,2}$ would be a subset of those reducing k_{cat}/K_m^{chem} because k_{cat}/K_m^{chem} includes both a phosphoryl transfer chemical step and an additional step (binding). Consistent with this expectation, mutations affect either k_{cat}/K_m^{chem} alone or k_{cat}/K_m^{chem} and $k_{chem,2}$ to a similar or smaller extent (Fig. 7C).

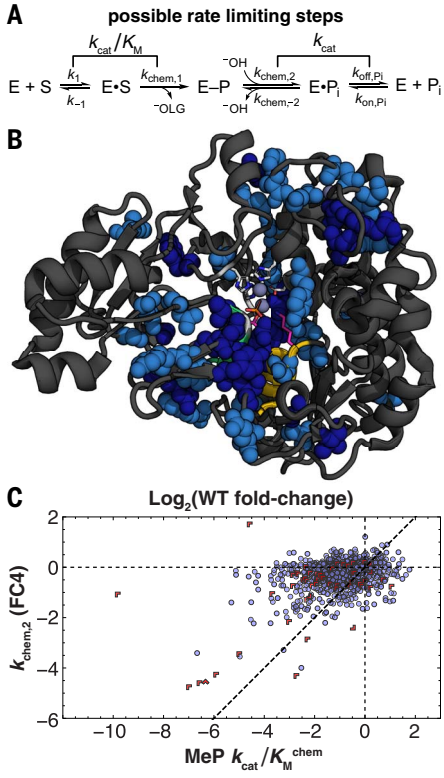

Fig. 7. FC4: Mutational effects on phosphoenzyme intermediate hydrolysis. (**A**) Schematic of PafA catalytic cycle with possible rate-limiting steps under saturating (k_{cat}) and subsaturating (k_{cat}/K_m) conditions. (**B**) Structure showing positions with decreased $k_{chem,2}$ ($P < 0.05$ and $P < 0.1$ in dark and light blue, respectively) upon mutation (spheres). Positions lacking an estimate of $k_{chem,2}$ for both substitutions are light gray ribbons, and positions without significant effects are black ribbons. (**C**) Scatter plot comparing mutational effects on phosphoenzyme hydrolysis ($k_{chem,2}$, or FC4) and k_{cat}/K_m^{chem}. Limits are indicated with red chevrons pointing in limit directions (supplementary text S6).

Discussion

HT-MEK uses automatic valved microfluidics to carry out high-throughput expression, purification, and comprehensive biochemical characterization of enzymes at unprecedented scale and mechanistic depth. In the future, HT-MEK can be applied to the vast number of enzymes whose activity can be monitored through fluorescence directly or with a coupled assay. In particular, the ability to sensitively detect P_i (*18*) renders HT-MEK immediately applicable to adenosine triphosphatases, guanosine triphosphatases, helicases, protein chaperones, polymerases (with pyrophosphatase present), and many others.

Deleterious effects throughout the enzyme and at the surface, with many of the largest effects distant from the active site, mirror results obtained from DMS studies of other enzymes that often reveal distal effects on product formation or organismal fitness (*12*, *59*–*61*). However, the ability of HT-MEK to provide quantitative measurements of a battery of kinetic and thermodynamic parameters yields an atlas of PafA functional "architecture" with unprecedented detail (table S17). Regions of residues with similar catalytic signatures extending throughout the enzyme affirm that the enzyme beyond the active site is not a passive, monolithic scaffold but rather contributes to function in multiple ways.

Comparing patterns of mutational effects between FCs reveals that these architectural solutions are idiosyncratic. For example, K162/R164, and the T79 nucleophile, sit at the N-termini of their respective helices, but the largest FC2 effects were on and around the nucleophile helix, whereas FC1 effects were not similarly distributed around the monoesterase helix. This

difference perhaps reflects a need for more interactions to secure the nucleophile helix against ground-state electrostatic repulsive forces. Twice as many glycine as valine mutations increased P_i binding (fig. S58), potentially because side-chain ablation allows structural rearrangements to reduce electrostatic repulsion without disrupting favorable binding interactions.

The need for interactions throughout the enzyme for optimal catalysis highlights the challenges inherent in de novo enzyme design because it suggests that computational efforts must consider in detail the interactions of a prohibitively large number of residues. The detailed architectural maps provided by HT-MEK can focus computational and experimental mutagenesis by distinguishing catalytic from folding effects and by identifying residues and regions that affect particular aspects of catalysis.

The presence of a long-lived inactive population of many PafA variants emphasizes how different underlying (and unexpected) biophysical mechanisms can compromise an enzyme's activity and thus the need to explicitly decouple effects on folding and catalysis to understand function. Analogous behavior observed for these mutants in *E. coli* is consistent with selective pressure to avoid misfolding in vivo and adds to growing evidence that kinetic factors affect stable protein expression in cells (*20*, *30*, *62*–*64*). We speculate that highly stable proteins such as PafA and other secreted enzymes may be more prone to forming kinetically trapped states.

Although PafA functional regions have superficial similarities to sectors and other measures of evolutionary covariation and coconservation (*65*–*69*), our data report on sequence-function relationships in ways that sequence analyses alone cannot. On the basis of a metagenomic alignment of 14,505 PafA-like AP superfamily sequences (fig. S67 and supplementary text S7), we found that observed k_{cat}/K_m values correlate only modestly with conservation at a given position (figs. S68 and S69). Positions at which mutations promote misfolding tend to be most conserved, suggesting that the largest selective pressure at the residue level may be related to ensuring correct folding, whereas correlations between individual FCs and conservation are weak, with many large effects at nonconserved residues (figs. S69 and S70). For PafA, selective pressures will differ with the available P_i at the organism's physical location, whether available P_i varies temporally, and whether there is competition for P_i from other organisms in the same ecological niche. Residues with critical roles in responding to these adaptive pressures would be poorly conserved, changing frequently despite being tightly linked to survival. These results underscore the need for in-depth functional studies to uncover the relationships between the evolution of particular functions and conservation.

Enzymes are the targets of many therapeutics, are altered in genetic diseases, serve as tools for molecular biology, and play critical roles in industrial processes. Its rapidity and low cost make HT-MEK a powerful tool for future applications across all these areas. In basic research, the large, highly quantitative datasets provided by HT-MEK can greatly extend and even supplant traditional SDM approaches for the initial characterization of new enzymes and for in-depth mechanistic investigation. Combined with recent advances in gene synthesis, HT-MEK can rapidly functionally characterize metagenomic variants, providing a critically needed dimension to phylogenetic analyses. In medicine, we anticipate that HT-MEK will rapidly determine the functional effects of human enzyme allelic variants of unknown relevance identified from sequence data and systematically identify candidate allosteric surfaces within currently "undruggable" therapeutic target enzymes. We anticipate HT-MEK contributing to these and still more areas of basic and applied biology, medicine, and engineering.

Materials and methods summary

A full description of materials and methods is provided in the supplementary materials. Briefly, we fabricated microfluidic devices and aligned them to plasmid DNA arrays as previously described (*70*–*72*), then connected devices to a custom pneumatic manifold (*73*) and imaged using a fully automated fluorescence microscope. The plasmid DNAs coded for a set of specified PafA variants, each with a C-terminal eGFP tag. The PafA-eGFP variants were expressed in vitro on-chip and immobilized to Button valves by means of antibodies to eGFP (*72*) in parallel, before quantification of the enzyme concentration within each chamber by using an eGFP standard curve. This entire process takes ~10 hours to complete. Before measuring kinetics of substrate hydrolysis for cMUP, MeP, and MecMUP, we determined product standard curves for each chamber by introducing a series of product concentrations [cMU for cMUP and MecMUP hydrolysis and P_i in the presence of 30 μM of modified PBP (*18*) for MeP hydrolysis], imaging the device after each addition. To measure rates of hydrolysis, we flowed a single concentration of substrate into the device with the Button valves closed and then started reactions by (i) closing the Sandwich valves to isolate individual reaction chambers and (ii) opening the Button valves to expose the immobilized enzyme within each chamber to substrate. We quantified initial rates of product formation for each chamber by imaging over time across the entire device and converting measured intensities to product concentrations using standard curves. To determine k_{cat}, K_m, and k_{cat}/K_m for cMUP hydrolysis and k_{cat}/K_m for MeP and MecMUP hydrolysis, we quantified initial rates of product formation for a series of increasing substrate concentrations, scaled rates by measured enzyme concentration, and fit to a simple Michaelis-Menten model. For the nonfluorogenic MeP substrate, we detected formation of P_i by performing reactions in the presence of 30 μM PBP. To determine the K_i for P_i inhibition, we assayed rates of cMUP hydrolysis at 10 or 50 μM cMUP in the presence of increasing P_i concentration, fit initial rates as described above, and then fit these rates to a competitive inhibition model. For each assay type, we carried out multiple replicate experiments for each parameter for each mutant, allowing us to perform extensive quality control measurements and determine the statistical significance of effects.

REFERENCES AND NOTES

1. Q. Wang *et al.*, Landscape of multi-nucleotide variants in 125,748 human exomes and 15,708 genomes. *Nat. Commun.* **11**, 2539 (2020). doi: 10.1038/s41467-019-12438-5; pmid: 32461613
2. M. Claussnitzer *et al.*, A brief history of human disease genetics. *Nature* **577**, 179–189 (2020). doi: 10.1038/s41586-019-1879-7; pmid: 31915397
3. M. Lek *et al.*, Analysis of protein-coding genetic variation in 60,706 humans. *Nature* **536**, 285–291 (2016). doi: 10.1038/nature19057; pmid: 27535533
4. A. Stein, D. M. Fowler, R. Hartmann-Petersen, K. Lindorff-Larsen, Biophysical and mechanistic models for disease-causing protein variants. *Trends Biochem. Sci.* **44**, 575–588 (2019). doi: 10.1016/j.tibs.2019.01.003; pmid: 30712981
5. J. B. Kinney, D. M. McCandlish, Massively parallel assays and quantitative sequence-function relationships. *Annu. Rev. Genomics Hum. Genet.* **20**, 99–127 (2019). doi: 10.1146/annurev-genom-083118-014845; pmid: 31091417
6. C. Blanco, E. Janzen, A. Pressman, R. Saha, I. A. Chen, Molecular fitness landscapes from high-coverage sequence profiling. *Annu. Rev. Biophys.* **48**, 1–18 (2019). doi: 10.1146/annurev-biophys-052118-115333; pmid: 30601678
7. J. Weile, F. P. Roth, Multiplexed assays of variant effects contribute to a growing genotype-phenotype atlas. *Hum. Genet.* **137**, 665–678 (2018). doi: 10.1007/s00439-018-1916-x; pmid: 30073413
8. G. P. Lisi, J. P. Loria, Allostery in enzyme catalysis. *Curr. Opin. Struct. Biol.* **47**, 123–130 (2017). doi: 10.1016/j.sbi.2017.08.002; pmid: 28865247
9. K. A. Reynolds, R. N. McLaughlin, R. Ranganathan, Hot spots for allosteric regulation on protein surfaces. *Cell* **147**, 1564–1575 (2011). doi: 10.1016/j.cell.2011.10.049; pmid: 22196731
10. D. A. Keedy *et al.*, An expanded allosteric network in PTP1B by multitemperature crystallography, fragment screening, and covalent tethering. *eLife* **7**, e36307 (2018). doi: 10.7554/eLife.36307; pmid: 29877794
11. D. M. Fowler *et al.*, High-resolution mapping of protein sequence-function relationships. *Nat. Methods* **7**, 741–746 (2010). doi: 10.1038/nmeth.1492; pmid: 20711194
12. C. L. Araya, D. M. Fowler, Deep mutational scanning: Assessing protein function on a massive scale. *Trends Biotechnol.* **29**, 435–442 (2011). doi: 10.1016/j.tibtech.2011.04.003; pmid: 21561674
13. J. K. Lassila, J. G. Zalatan, D. Herschlag, Biological phosphoryl-transfer reactions: Understanding mechanism and catalysis. *Annu. Rev. Biochem.* **80**, 669–702 (2011). doi: 10.1146/annurev-biochem-060409-092741; pmid: 21513457
14. P. M. Fordyce *et al.*, De novo identification and biophysical characterization of transcription-factor binding sites with microfluidic affinity analysis. *Nat. Biotechnol.* **28**, 970–975 (2010). doi: 10.1038/nbt.1675; pmid: 20802496

15. S. J. Maerkl, S. R. Quake, A systems approach to measuring the binding energy landscapes of transcription factors. *Science* **315**, 233–237 (2007). doi: 10.1126/science.1131007; pmid: 17218526
16. F. Sunden *et al*., Mechanistic and evolutionary insights from comparative enzymology of phosphomonoesterases and phosphodiesterases across the alkaline phosphatase superfamily. *J. Am. Chem. Soc.* **138**, 14273–14287 (2016). doi: 10.1021/jacs.6b06186; pmid: 27670607
17. M. M. Santoro, D. W. Bolen, Unfolding free energy changes determined by the linear extrapolation method. 1. Unfolding of phenylmethanesulfonyl α-chymotrypsin using different denaturants. *Biochemistry* **27**, 8063–8068 (1988). doi: 10.1021/bi00421a014; pmid: 3233195
18. M. Brune, J. L. Hunter, J. E. T. Corrie, M. R. Webb, Direct, real-time measurement of rapid inorganic phosphate release using a novel fluorescent probe and its application to actomyosin subfragment 1 ATPase. *Biochemistry* **33**, 8262–8271 (1994). doi: 10.1021/bi00193a013; pmid: 8031761
19. P. J. O'Brien, D. Herschlag, Alkaline phosphatase revisited: Hydrolysis of alkyl phosphates. *Biochemistry* **41**, 3207–3225 (2002). doi: 10.1021/bi012166y; pmid: 11863460
20. R. M. Addabbo *et al*., Complementary role of co- and post-translational events in de novo protein biogenesis. *J. Phys. Chem. B* **124**, 6488–6507 (2020). doi: 10.1021/acs.jpcb.0c03039; pmid: 32456434
21. J. M. Sturtevant, M. H. Yu, C. Haase-Pettingell, J. King, Thermostability of temperature-sensitive folding mutants of the P22 tailspike protein. *J. Biol. Chem.* **264**, 10693–10698 (1989). doi: 10.1016/S0021-9258(18)81678-7; pmid: 2525128
22. M. Guo, Y. Xu, M. Gruebele, Temperature dependence of protein folding kinetics in living cells. *Proc. Natl. Acad. Sci. U.S.A.* **109**, 17863–17867 (2012). doi: 10.1073/pnas.1201797109; pmid: 22665776
23. D. H. Smith, J. King, Temperature-sensitive mutants blocked in the folding or subunit assembly of the bacteriophage P22 tail spike protein. III. Intensive polypeptide chains synthesized at 39°C. *J. Mol. Biol.* **145**, 653–676 (1981). doi: 10.1016/0022-2836(81)90308-9; pmid: 7265218
24. D. Baker, J. L. Sohl, D. A. Agard, A protein-folding reaction under kinetic control. *Nature* **356**, 263–265 (1992). doi: 10.1038/356263a0; pmid: 1552947
25. H. Im, M.-S. Woo, K. Y. Hwang, M.-H. Yu, Interactions causing the kinetic trap in serpin protein folding. *J. Biol. Chem.* **277**, 46347–46354 (2002). doi: 10.1074/jbc.M207682200; pmid: 12244055
26. C. Park, S. Marqusee, Probing the high energy states in proteins by proteolysis. *J. Mol. Biol.* **343**, 1467–1476 (2004). doi: 10.1016/j.jmb.2004.08.085; pmid: 15491624
27. S. Thompson, Y. Zhang, C. Ingle, K. A. Reynolds, T. Kortemme, Altered expression of a quality control protease in *E. coli* reshapes the in vivo mutational landscape of a model enzyme. *eLife* **9**, e53476 (2020). doi: 10.7554/eLife.53476; pmid: 32701056
28. T. Gidalevitz, V. Prahlad, R. I. Morimoto, The stress of protein misfolding: From single cells to multicellular organisms. *Cold Spring Harb. Perspect. Biol.* **3**, a009704–a009704 (2011). doi: 10.1101/cshperspect.a009704; pmid: 21536706
29. J. L. Sohl, S. S. Jaswal, D. A. Agard, Unfolded conformations of α-lytic protease are more stable than its native state. *Nature* **395**, 817–819 (1998). doi: 10.1038/27470; pmid: 9796818
30. S. S. Jaswal, J. L. Sohl, J. H. Davis, D. A. Agard, Energetic landscape of α-lytic protease optimizes longevity through kinetic stability. *Nature* **415**, 343–346 (2002). doi: 10.1038/415343a; pmid: 11797014
31. A. L. Watters *et al*., The highly cooperative folding of small naturally occurring proteins is likely the result of natural selection. *Cell* **128**, 613–624 (2007). doi: 10.1016/j.cell.2006.12.042; pmid: 17289578
32. F. Bemporad *et al*., Biological function in a non-native partially folded state of a protein. *EMBO J.* **27**, 1525–1535 (2008). doi: 10.1038/emboj.2008.82; pmid: 18451804
33. R. E. Jefferson, T. M. Blois, J. U. Bowie, Membrane proteins can have high kinetic stability. *J. Am. Chem. Soc.* **135**, 15183–15190 (2013). doi: 10.1021/ja407232b; pmid: 24032628
34. J. G. Zalatan, T. D. Fenn, D. Herschlag, Comparative enzymology in the alkaline phosphatase superfamily to determine the catalytic role of an active-site metal ion. *J. Mol. Biol.* **384**, 1174–1189 (2008). doi: 10.1016/j.jmb.2008.09.059; pmid: 18851975
35. L. D. Andrews, T. D. Fenn, D. Herschlag, Ground state destabilization by anionic nucleophiles contributes to the activity of phosphoryl transfer enzymes. *PLOS Biol.* **11**, e1001599 (2013). doi: 10.1371/journal.pbio.1001599; pmid: 23843744
36. D. Hilvert, Design of protein catalysts. *Annu. Rev. Biochem.* **82**, 447–470 (2013). doi: 10.1146/annurev-biochem-072611-101825; pmid: 23746259
37. M. I. Freiberger, A. B. Guzovsky, P. G. Wolynes, R. G. Parra, D. U. Ferreiro, Local frustration around enzyme active sites. *Proc. Natl. Acad. Sci. U.S.A.* **116**, 4037–4043 (2019). doi: 10.1073/pnas.1819859116; pmid: 30765513
38. K. L. Morley, R. J. Kazlauskas, Improving enzyme properties: When are closer mutations better? *Trends Biotechnol.* **23**, 231–237 (2005). doi: 10.1016/j.tibtech.2005.03.005; pmid: 15866000
39. O. Dagliyan, N. V. Dokholyan, K. M. Hahn, Engineering proteins for allosteric control by light or ligands. *Nat. Protoc.* **14**, 1863–1883 (2019). doi: 10.1038/s41596-019-0165-3; pmid: 31076662
40. J. W. McCormick, D. Pincus, O. Resnekov, K. A. Reynolds, Strategies for engineering and rewiring kinase regulation. *Trends Biochem. Sci.* **45**, 259–271 (2020). doi: 10.1016/j.tibs.2019.11.005; pmid: 31866305
41. K. Gunasekaran, B. Ma, R. Nussinov, Is allostery an intrinsic property of all dynamic proteins? *Proteins* **57**, 433–443 (2004). doi: 10.1002/prot.20232; pmid: 15382234
42. J. A. Hardy, J. A. Wells, Searching for new allosteric sites in enzymes. *Curr. Opin. Struct. Biol.* **14**, 706–715 (2004). doi: 10.1016/j.sbi.2004.10.009; pmid: 15582395
43. G. R. Bowman, E. R. Bolin, K. M. Hart, B. C. Maguire, S. Marqusee, Discovery of multiple hidden allosteric sites by combining Markov state models and experiments. *Proc. Natl. Acad. Sci. U.S.A.* **112**, 2734–2739 (2015). doi: 10.1073/pnas.1417811112; pmid: 25730859
44. F. Sunden, A. Peck, J. Salzman, S. Ressl, D. Herschlag, Extensive site-directed mutagenesis reveals interconnected functional units in the alkaline phosphatase active site. *eLife* **4**, e06181 (2015). doi: 10.7554/eLife.06181; pmid: 25902402
45. P. J. Carter, G. Winter, A. J. Wilkinson, A. R. Fersht, The use of double mutants to detect structural changes in the active site of the tyrosyl-tRNA synthetase (*Bacillus stearothermophilus*). *Cell* **38**, 835–840 (1984). doi: 10.1016/0092-8674(84)90278-2; pmid: 6488318
46. P. Carter, J. A. Wells, Dissecting the catalytic triad of a serine protease. *Nature* **332**, 564–568 (1988). doi: 10.1038/332564a0; pmid: 3282170
47. D. Herschlag, A. Natarajan, Fundamental challenges in mechanistic enzymology: Progress toward understanding the rate enhancements of enzymes. *Biochemistry* **52**, 2050–2067 (2013). doi: 10.1021/bi4000113; pmid: 23488725
48. W. P. Jencks, Mechanism of enzyme action. *Annu. Rev. Biochem.* **32**, 639–676 (1963). doi: 10.1146/annurev.bi.32.070163.003231; pmid: 14140708
49. A. R. Fersht, *Enzyme Structure and Mechanism* (W.H. Freeman and Co., ed. 2, 1985).
50. W. P. Jencks, Binding energy, specificity, and enzymic catalysis: The Circe effect. *Adv. Enzymol. Relat. Areas Mol. Biol.* **43**, 219–410 (1975). doi: 10.1002/9780470122884.ch4; pmid: 892
51. L. D. Andrews, H. Deng, D. Herschlag, Isotope-edited FTIR of alkaline phosphatase resolves paradoxical ligand binding properties and suggests a role for ground-state destabilization. *J. Am. Chem. Soc.* **133**, 11621–11631 (2011). doi: 10.1021/ja203370b; pmid: 21692505
52. W. J. Albery, J. R. Knowles, Evolution of enzyme function and the development of catalytic efficiency. *Biochemistry* **15**, 5631–5640 (1976). doi: 10.1021/bi00670a032; pmid: 999839
53. F. M. Menger, Analysis of ground-state and transition-state effects in enzyme catalysis. *Biochemistry* **31**, 5368–5373 (1992). doi: 10.1021/bi00138a018; pmid: 1606161
54. J. D. McCarter, M. J. Adam, S. G. Withers, Binding energy and catalysis. Fluorinated and deoxygenated glycosides as mechanistic probes of Escherichia coli (lacZ) β-galactosidase. *Biochem. J.* **286**, 721–727 (1992). doi: 10.1042/bj2860721; pmid: 1417731
55. S. A. Moore, W. P. Jencks, Formation of active site thiol esters of CoA transferase and the dependence of catalysis on specific binding interactions. *J. Biol. Chem.* **257**, 10893–10907 (1982). doi: 10.1016/S0021-9258(18)33908-5; pmid: 6955308
56. A. Whitty, C. A. Fierke, W. P. Jencks, Role of binding energy with coenzyme A in catalysis by 3-oxoacid coenzyme A transferase. *Biochemistry* **34**, 11678–11689 (1995). doi: 10.1021/bi00037a005; pmid: 7547900
57. Y.-L. Zhang *et al*., Impaired transition state complementarity in the hydrolysis of O-arylphosphorothioates by protein-tyrosine phosphatases. *Biochemistry* **38**, 12111–12123 (1999). doi: 10.1021/bi990836i; pmid: 10508416
58. W. E. Hull, S. E. Halford, H. Gutfreund, B. D. Sykes, Phosphorus-31 nuclear magnetic resonance study of alkaline phosphatase: The role of inorganic phosphate in limiting the enzyme turnover rate at alkaline pH. *Biochemistry* **15**, 1547–1561 (1976). doi: 10.1021/bi00652a028; pmid: 4092
59. E. E. Wrenbeck, L. R. Azouz, T. A. Whitehead, Single-mutation fitness landscapes for an enzyme on multiple substrates reveal specificity is globally encoded. *Nat. Commun.* **8**, 15695 (2017). doi: 10.1038/ncomms15695; pmid: 28585537
60. J. R. Klesmith, J.-P. Bacik, E. E. Wrenbeck, R. Michalczyk, T. A. Whitehead, Trade-offs between enzyme fitness and solubility illuminated by deep mutational scanning. *Proc. Natl. Acad. Sci. U.S.A.* **114**, 2265–2270 (2017). doi: 10.1073/pnas.1614437114; pmid: 28196882
61. P. Bandaru *et al*., Deconstruction of the Ras switching cycle through saturation mutagenesis. *eLife* **6**, e27810 (2017). doi: 10.7554/eLife.27810; pmid: 28686159
62. C. M. Dobson, Protein folding and misfolding. *Nature* **426**, 884–890 (2003). doi: 10.1038/nature02261; pmid: 14685248
63. M. S. Faber, E. E. Wrenbeck, L. R. Azouz, P. J. Steiner, T. A. Whitehead, Impact of in vivo protein folding probability on local fitness landscapes. *Mol. Biol. Evol.* **36**, 2764–2777 (2019). doi: 10.1093/molbev/msz184; pmid: 31400199
64. V. Zhao, W. M. Jacobs, E. I. Shakhnovich, Effect of protein structure on evolution of cotranslational folding. *Biophys. J.* **119**, 1123–1134 (2020). doi: 10.1016/j.bpj.2020.06.037; pmid: 32857962
65. N. Halabi, O. Rivoire, S. Leibler, R. Ranganathan, Protein sectors: Evolutionary units of three-dimensional structure. *Cell* **138**, 774–786 (2009). doi: 10.1016/j.cell.2009.07.038; pmid: 19703402
66. O. Rivoire, K. A. Reynolds, R. Ranganathan, Evolution-based functional decomposition of proteins. *PLOS Comput. Biol.* **12**, e1004817 (2016). doi: 10.1371/journal.pcbi.1004817; pmid: 27254668
67. V. H. Salinas, R. Ranganathan, Coevolution-based inference of amino acid interactions underlying protein function. *eLife* **7**, e34300 (2018). doi: 10.7554/eLife.34300; pmid: 30024376
68. T. Teşileanu, L. J. Colwell, S. Leibler, Protein sectors: Statistical coupling analysis versus conservation. *PLOS Comput. Biol.* **11**, e1004091 (2015). doi: 10.1371/journal.pcbi.1004091; pmid: 25723535
69. P. Creixell *et al*., Hierarchical organization endows the kinase domain with regulatory plasticity. *Cell Syst.* **7**, 371–383.e4 (2018). doi: 10.1016/j.cels.2018.08.008; pmid: 30243563
70. P. M. Fordyce *et al*., Basic leucine zipper transcription factor Hac1 binds DNA in two distinct modes as revealed by microfluidic analyses. *Proc. Natl. Acad. Sci. U.S.A.* **109**, E3084–E3093 (2012). doi: 10.1073/pnas.1212457109; pmid: 23054834
71. D. D. Le *et al*., Comprehensive, high-resolution binding energy landscapes reveal context dependencies of transcription factor binding. *Proc. Natl. Acad. Sci. U.S.A.* **115**, E3702–E3711 (2018). doi: 10.1073/pnas.1715888115; pmid: 29588420
72. A. K. Aditham, C. J. Markin, D. A. Mokhtari, N. DelRosso, P. M. Fordyce, High-throughput affinity measurements of transcription factor and DNA mutations reveal affinity and specificity determinants. *Cell Syst.* **12**, 112–127.e11 (2021). doi: 10.1016/j.cels.2020.11.012; pmid: 33340452
73. K. Brower *et al*., An open-source, programmable pneumatic setup for operation and automated control of single- and multi-layer microfluidic devices. *HardwareX* **3**, 117–134 (2018). doi: 10.1016/j.ohx.2017.10.001; pmid: 30221210
74. C. J. Markin *et al*., Revealing enzyme functional architecture via high-throughput microfluidic enzyme kinetics. Open Science Repository (2021); doi: 10.17605/OSF.IO/QRN3C

ACKNOWLEDGMENTS

We thank members of the Herschlag and Fordyce laboratories for discussions and review of the manuscript, M. Madsen for technical assistance, K. Brower for microfluidic mold fabrication and optics assistance, and S. Costello and S. Marqusee for helpful discussions. **Funding:** This research was supported by the NIH grant R01 (GM064798) awarded to D.H. and P.M.F., a Joint Initiative for Metrology in Biology (JIMB) seed grant, a Stanford Bio-X Interdisciplinary Initiative Seed Grant, an Ono Pharma Foundation Breakthrough Innovation Prize, and the Gordon and Betty Moore Foundation (grant 8415). P.M.F. acknowledges the support of an Alfred P. Sloan Foundation fellowship and is a Chan Zuckerberg Biohub Investigator. C.J.M. acknowledges the support of a Canadian Institutes of Health Research (CIHR) Postdoctoral Fellowship. D.A.M. acknowledges support from the Stanford Medical Scientist Training Program

and a Stanford Interdisciplinary Graduate Fellowship (Anonymous Donor) affiliated with Stanford ChEM-H. E.A. acknowledges support from the NIH (GM0595). This research used resources of the National Energy Research Scientific Computing Center (NERSC), a US Department of Energy (DOE) Office of Science User Facility operated under contract DE-AC02-05CH11231, as well as resources obtained from the Facilities Integrating Collaborations for User Science (FICUS) program associated with the Joint Genome Institute of the DOE, proposal 503369. **Author contributions:** C.J.M., D.A.M., and F.S. designed experiments and collected and analyzed data. M.J.A. collected and analyzed data. C.S. provided assistance with statistical analyses. D.A.M. and E.A. generated the sequence alignments and performed phylogenetic analyses. S.A.L. contributed to hardware automation and software development. D.H. and P.M.F. conceived and supervised the project and acquired funding. C.J.M., D.A.M., D.H., and P.M.F. wrote and revised the manuscript, with input from all authors. **Competing interests:** The authors declare no competing financial interests. **Data and materials availability:** Summary tables of all kinetic and thermodynamic parameters measured for each mutant are included in the supplementary materials. All data acquired in this study, all code used to obtain and process images and fit kinetic and thermodynamic parameters, and PyMOL files corresponding to all figures containing structural information are available in a registered Open Science Foundation Repository (DOI: 10.17605/OSF.IO/QRN3C) (*74*). Additional per-experiment and per-mutant summary PDFs are available on the Fordyce Lab website (www.fordycelab.com/publication-data).

SUPPLEMENTARY MATERIALS

science.sciencemag.org/content/373/6553/eabf8761/suppl/DC1
Materials and Methods
Supplementary Text
Figs. S1 to S70
Tables S1 to S17
References (*75*–*118*)
MDAR Reproducibility Checklist
Data files S1 and S2

View/request a protocol for this paper from *Bio-protocol*.

25 November 2020; accepted 24 May 2021
10.1126/science.abf8761

Revealing enzyme functional architecture via high-throughput microfluidic enzyme kinetics

C. J. Markin, D. A. Mokhtari, F. Sunden, M. J. Appel, E. Akiva, S. A. Longwell, C. Sabatti, D. Herschlag and P. M. Fordyce

Science **373** (6553), eabf8761.
DOI: 10.1126/science.abf8761

Go big or you'll get lost

Rational mutagenesis is a common approach to investigating or engineering enzyme function in vitro, but the ease with which one can manipulate protein sequences belies many pitfalls in connecting sparse activity data to an enzyme's true functional landscape. Using a high-throughput platform, Markin *et al.* expressed, purified, and performed an array of kinetic measurements on a target esterase, collecting data from >1000 mutations spanning the entire protein (see the Perspective by Baumer and Whitehead). Protein misfolding into an inactive state, rather than decreased equilibrium stability, was a crucial factor in negatively affected variants spread throughout the protein. When combined with prior mechanistic understanding and structures, four "functional components" help to rationalize the otherwise complex spatial pattern of effects of mutations on different aspects of enzyme function, all of which would be invisible from mutagenesis of just a few residues.

Science, abf8761, this issue p. eabf8761; see also abj8346, p. 391

Available online at www.sciencedirect.com

ScienceDirect

Current Opinion in Structural Biology

High throughput and quantitative enzymology in the genomic era

D. A. Mokhtari[1,a], M. J. Appel[1,a], P. M. Fordyce[2,4,5,6] and D. Herschlag[1,3,4]

Abstract

Accurate predictions from models based on physical principles are the ultimate metric of our biophysical understanding. Although there has been stunning progress toward structure prediction, quantitative prediction of enzyme function has remained challenging. Realizing this goal will require large numbers of quantitative measurements of rate and binding constants and the use of these ground-truth data sets to guide the development and testing of these quantitative models. Ground truth data more closely linked to the underlying physical forces are also desired. Here, we describe technological advances that enable both types of ground truth measurements. These advances allow classic models to be tested, provide novel mechanistic insights, and place us on the path toward a predictive understanding of enzyme structure and function.

Addresses

[1] Department of Biochemistry, Stanford University, Stanford, CA, 94305, USA
[2] Department of Bioengineering, Stanford University, Stanford, CA, 94305, USA
[3] Department of Chemical Engineering, Stanford University, Stanford, CA, 94305, USA
[4] ChEM-H Institute, Stanford University, Stanford, CA, 94305, USA
[5] Department of Genetics, Stanford University, Stanford, CA, 94305, USA
[6] Chan Zuckerberg Biohub San Francisco, CA, 94110, USA

Corresponding authors: Herschlag, D (herschla@stanford.edu); Fordyce, P.M (pfordyce@stanford.edu)
[a] These authors contributed equally to this work.

Current Opinion in Structural Biology 2021, **71**:259–273

This review comes from a themed issue on **Catalysis and Regulation**

Edited by **Ruth Nussinov** and **Mikako Shirouzu**

For a complete overview see the Issue and the Editorial

https://doi.org/10.1016/j.sbi.2021.07.010

Introduction

Scientists can now predict and design protein structure with ångström accuracy, a triumph culminating from decades of experimental and computational efforts [1,2]. In this perspective, we describe why the approaches that have been so successful in protein design are unlikely to lead to analogously predictive models for protein function, and we introduce concepts and experimental approaches that address these limitations and move us toward the ultimate goals of accurately and quantitatively predicting and designing function.

Structure broadly and deeply informs our understanding of function — consider the striking visualizations of motor proteins that have revealed the lever arms of myosin, dynein, and kinesin and their ATP-dependent power strokes [3], and the myriad of proteins whose shape is integral to their function, such as the β-clamp that encircles DNA to enhance polymerase processivity [4]. Nevertheless, more than structure is needed to describe, understand, and quantitatively predict function. Indeed, many proteins with the same fold differ in function, quantitively and even qualitatively [5].

Function involves a series of states, such as the conformations through the myosin reaction cycle or the states in chemical reactions catalyzed by enzymes (substrate binding (E•S), transition state (E•S‡), product complex (E•P), and release (E + P) to regenerate free enzyme ready for another round of catalysis). A minimal description of protein function therefore requires describing these states and determining the rate and equilibrium constants that define their transition probabilities and relative populations, respectively.

But still, more is required to understand and ultimately predict and design new functions — an ability to specify the functional consequences of sequence changes. Enzymes are large, with residues beyond the active site required for function, minimally to fold into and stabilize the correct binding and active site configurations [6]. But regions far from the active site can also have considerable functional consequences [7], as evidenced by allosteric modulation [8,9] and remote mutational effects frequently identified in high-throughput screens [10–12]. To find and describe which residues, sets of residues, and substructures affect function, as well as the particular aspects of function that are affected, we need approaches to systematically interrogate all residues and to determine the effects of perturbing them

through each step of the enzyme's reaction cycle. In other words, we need to measure many rate and equilibrium constants for many mutants. Here, we highlight a breakthrough approach that allows these measurements to be made.

In principle, with sufficient empirical data, machine and deep learning approaches could be used to provide accurate, predictive models of enzyme function. However, sequence space is vast — so vast that nature has only sampled a miniscule corner of it [13]. And whereas pairwise residue information is largely sufficient to predict protein structure [14], enzyme function is much more complex, with multiple distal residues exerting functional effects on one another. These effects correspond mathematically to higher-order terms to account for the effects from combinations of multiple residues and are thus terms that are needed to quantitatively describe function. Because of this complexity, vast amounts of data would likely be required to define the relationship between sequence and function, and we suspect that the scale of data needed to predict enzyme function via machine learning and deep learning approaches may greatly exceed what is measurable, even with recent breakthroughs.

In contrast, physics-based approaches are scalable, so that simple rules can be used to describe the behavior of arbitrarily complex systems [15,16]. These models relate atomic forces and motions, captured by the preferred substates in conformational ensembles, to thermodynamic and kinetic constants. From the perspective of statistical mechanics, the constants that define function arise from the energy landscapes that define an ensemble of enzyme substates and the transition and reaction probabilities for each substate, represented mathematically in Figure 1 [17,18].

Thus, we need to go beyond structures to ensembles, and beyond structure—function relationships to ensemble—function relationships, and we will need to use experimental determinations of these relationships to test and build the physics-based models needed to quantitatively and accurately predict enzyme function. Here, we describe emerging X-ray crystallographic approaches that can provide this needed ensemble information.

Current design efforts yield enzymes that require cycles of randomization and selection to begin to approach natural enzymes. Perhaps the tortoise rather than the hare is needed to win this race [19], wherein large-scale quantitative and in-depth data are first collected and used to test and build models that will ultimately have the accuracy to predict and design enzyme function. We expect accurate enzyme functional prediction to remain a grand challenge of 21st-century biophysics — it is a still distant goal. Systematic blind tests of models built from large-scale quantitative data provide a promising, and perhaps necessary, path forward.

Ground truths are needed for model development

To develop and establish a model, 'ground truths' are needed. Ground truths are experimental data in a form that can be predicted by and thus compared to a model; without ground truths, there is no way to definitively test a model.

The most sophisticated models in enzymology combine quantum mechanics and molecular mechanics (QM/MM) and have been used to predict reaction rate constants [20,21]. However, in nearly all instances, the rate constants predicted by QM/MM were already measured and thus do not represent actual predictions that foretell a future event and that are incontrovertibly independent of the existing experimental findings [22]. The importance of predictions before measurement is underscored by the fact that the inability of protein folding models of the 1970s—1990s to predict structures was not apparent till they were challenged with truly blinded predictions (CASP, Critical Assessment of Structure Prediction); [1,23,24]). Ultimately, the algorithms and models that accurately predict structure were built using information from the large number of solved structures in the Protein Data Bank (PDB) [25], mining this information, and combining it with vast information from sequence conservation along with simplified energy potentials or rules derived via machine or deep learning [14,26—29,2].

Analogously, we need many measurements of kinetic and thermodynamic constants as ground truths to build and test predictive models of enzyme function, but current approaches are severely limited in their ability to deliver these essential data. Changes in residues throughout an enzyme can affect kinetic and thermodynamic constants, and combined changes will often not give additive effects; from a mathematical perspective, this property corresponds to a need for many terms in a model that can predict the effects from all sequence changes. With only a handful of measurements, there will not be enough data to constrain the model — from a simple algebraic standpoint, one needs the number of measurements to equal or exceed the number of variables in an equation to solve for those variables. Although we are unlikely to ever obtain sufficient measurements to fully define all of the variables of a master equation for function, we need many measurements to guide model development and then many predictions from these models — followed by many additional quantitative measurements — to provide a robust test of the models.

Structural ensembles can provide orthogonal ground truths. The relative occupancy of different

Figure 1

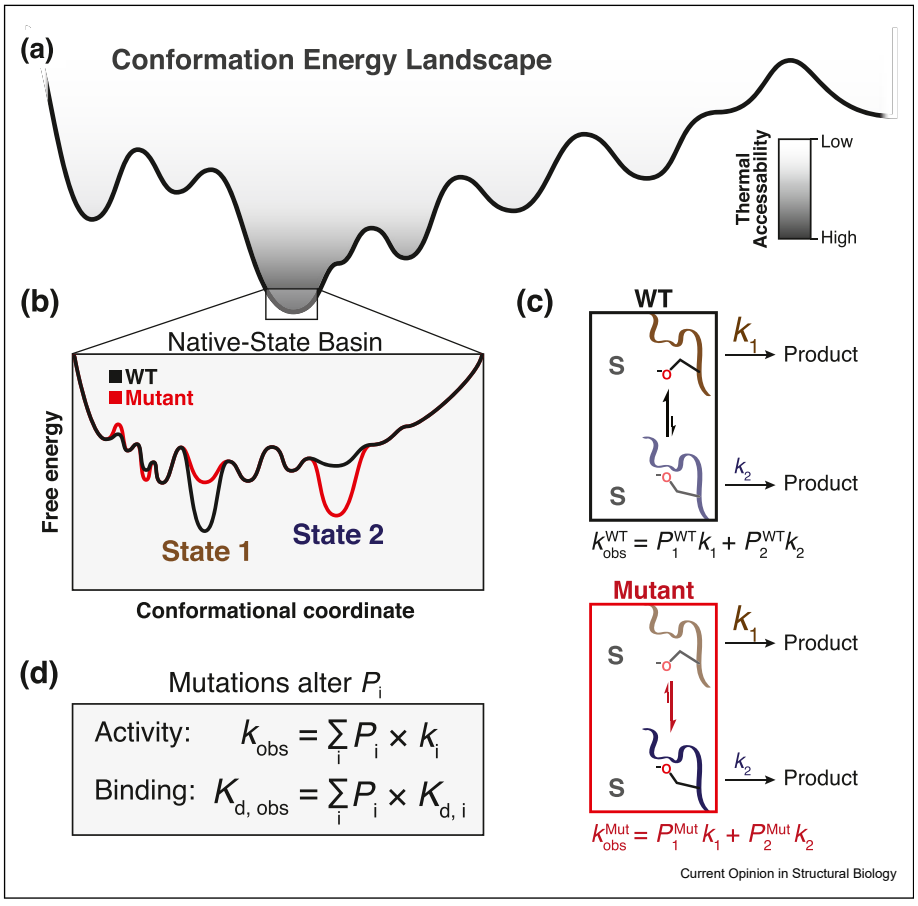

Enzymes function on a high-dimensional energy landscape. (a) Enzymes form a set of states specified by energy wells on a free energy landscape, with dimensionality defined by the thousands of degrees of freedom from each rotatable bond of each residue. **(b)** An example ensemble of near-energy substates in which State 1 (brown) and State 2 (blue) lie within the lowest energy basin ('native state basin') and equilibrate at room temperature. These substates have different intrinsic reactivities, reflecting barrier heights along the reaction coordinate that differ when projected from different conformational coordinates. **(c)** A mutation that does not affect intrinsic reactivity (red) can nevertheless diminish catalysis by redistributing equilibrium populations in the native state basin to favor less-active conformers (i.e. with higher free energy barriers to reaction; State 2 vs State 1). Mathematically, the apparent rate of the wild type (k_{obs}^{WT}) and mutant (k_{obs}^{Mut}) toward a substrate (S) is the probability-weighted (occupancy-weighted) sum of the intrinsic rate constants of each microscopic substate. In this two-state example, $k_1 > k_2$, so $k_{obs}^{WT} > k_{obs}^{Mut}$. **(d)** Observed enzymatic activity is the summed activity of each microscopic substate (k_i) weighted by its fractional occupancy (P_i). Mutations can alter the free energy landscape and change apparent activity (k_{obs}), or binding (K_d), by altering P_i, as shown in the figure, or by altering the reaction barrier (not shown).

conformational states reflects a balance of physical forces and thus provides ground truths that can be used as tests of models that account for these forces. Of further value, each ensemble provides a wealth of data — the distribution of states for each residue and around each backbone and sidechain bond, as well as information about their hydrogen bonds and electrostatic and van der Waals interactions. In contrast, average structures can be predicted without these 'details' being accurate, as evidenced by the rather simple force models present in successful Rosetta structural prediction algorithms [26,30].

The sections that follow describe recent advances in obtaining these ground truths for enzyme function.

The need for quantitative enzymology at scale

Recognizing the need for an immense amount of data to describe and understand enzymes and their function, high-throughput approaches have been used to interrogate up to $\sim 10^6$ sequence variants in parallel. In particular, deep mutational scanning (DMS) approaches have been applied to all possible single mutants for dozens of unique proteins [31,32].

Some DMS studies report the effects of mutations in a particular protein on organismal fitness, a convolution of multiple factors [33,34]. These experiments can also be designed to report more specific aspects of function, including catalytic efficiency, substrate specificity, stability, and interaction with binding partners [10,11,35–39].

Although valuable and sometimes of immediate practical benefit, these functional readouts still represent a convolution of contributing factors. For example, for observed catalytic function, a mutant enzyme down 100-fold in catalysis can be 99% unfolded, 99% partitioned to an alternative misfolded state, have a misaligned catalytic residue, have a binding interaction removed, or exhibit some combination of these factors. Thus, these functional readouts fall short of delivering the needed ground truths.

At the other end of the spectrum, traditional enzymology provides kinetic and thermodynamic constants that describe the catalytic cycle and have been combined with incisive mechanistic probes (e.g. alternative substrates, isotope effects, and so on) to provide deep mechanistic insights. However, these approaches are only feasible for a small number of variants of each enzyme. Past efforts to quantify properties of many variants in T4 lysozyme, pyruvate kinase, and β-glucosidase B underscore that data for many mutants can be collected when heroic means are used [40—43]. But even in these cases, the time and cost to carry out the additional measurements required to probe the mechanistic origins of the observed effects would be prohibitive.

It is hard to identify a discipline that has not been transformed at one time or another by a breakthrough technology. Here, technology was needed to efficiently provide the rich and quantitative data of traditional enzymology at a much larger scale for many variants and multiple enzymes.

Quantitative enzymology on a chip

Advances in microfluidics provided the opportunity to marry the strengths of traditional enzymology with automated high-throughput data collection and bring enzymology into the genomic age [44—46]. High-throughput microfluidic enzyme kinetics (HT-MEK; Figure 2) allows 1500 enzyme variants to be produced, purified, and subjected to multiple quantitative assays in days, at a miniscule fraction of the cost of traditional approaches [47].

Figure 2 outlines how HT-MEK experiments are performed. HT-MEK uses a microfluidic device with chambers aligned to a DNA microarray of 1500 isolated variant plasmids (Figure 2a). Expression and purification of enzyme variants are carried out in parallel, so that all 1500 enzymes can be purified, quantified, recruited to antibody-patterned surfaces, and ready for assay in hours (Figure 2b). Pneumatically controlled valves allow the user to protect the enzyme from flow-induced shear forces, while the expression solution is removed and an assay solution containing substrate is added to the chambers, followed by opening of the valves to simultaneously initiate reactions in all chambers (Figure 2c). Product formation is quantified over time via fluorescence, either directly using a fluorogenic substrate or indirectly using a coupled assay (Figure 2c). Once complete, reaction product is flowed out, and a new substrate stock is flowed in so that a series of assays can be performed iteratively. Figure 2d shows example Michaelis—Menten and inhibition curves obtained in HT-MEK experiments.

Each HT-MEK device can be used to carry out tens of reactions, and a single researcher can fabricate tens of devices in a day. These properties make it possible to carry out hundreds of assays — with multiple substrates, inhibitors, and solution conditions, as used traditionally in mechanistic enzymology — but to do so across thousands of enzyme variants and to do so in a few weeks. Thus, the properties of HT-MEK allow measurements of many kinetic and thermodynamic constants that provide valuable information about an enzyme and can serve as ground truths for model testing.

For PafA [48], a phosphate monoesterase and our test case, we obtained >6000 kinetic and thermodynamic constants from >650,000 kinetic measurements for 1036 mutants. HT-MEK provides a wide dynamic range, $\sim 10^5$ in rate for PafA, which allows measurement of large active site effects and reaction rates for noncognate substrates. High measurement precision is obtained with rigorous error estimates using bootstrapping, which is possible because of the many replicates acquired within each HT-MEK assay.

In addition to providing a large number of ground truth measurements that can be used to evaluate and guide the development of quantitative models, the initial PafA data provided extensive mechanistic information not previously accessible. The observation that mutations at most of the 526 PafA positions altered one or more kinetic and thermodynamic parameters underscores the need for measurements throughout an enzyme to map its function. Further revealing and displaying the intricacy of enzyme function, different sets of residues affected different reaction steps and underlying catalytic mechanisms as well as folding, as illustrated in the functional maps of Figure 3. The largest mutational effects were seen at the active site and directly around it, as expected, but effects extended from the active site all the way to the enzyme surface, with large effects many ångströms from the active site and different remote regions affecting different aspects of function (Figure 3a). We do not think that these effects could have been predicted a priori using current approaches. Regardless, researchers with predictive algorithms can now use those algorithms on any of the multiple enzymes amenable to HT-MEK, so that we can determine the algorithm's predictive power.

Figure 2

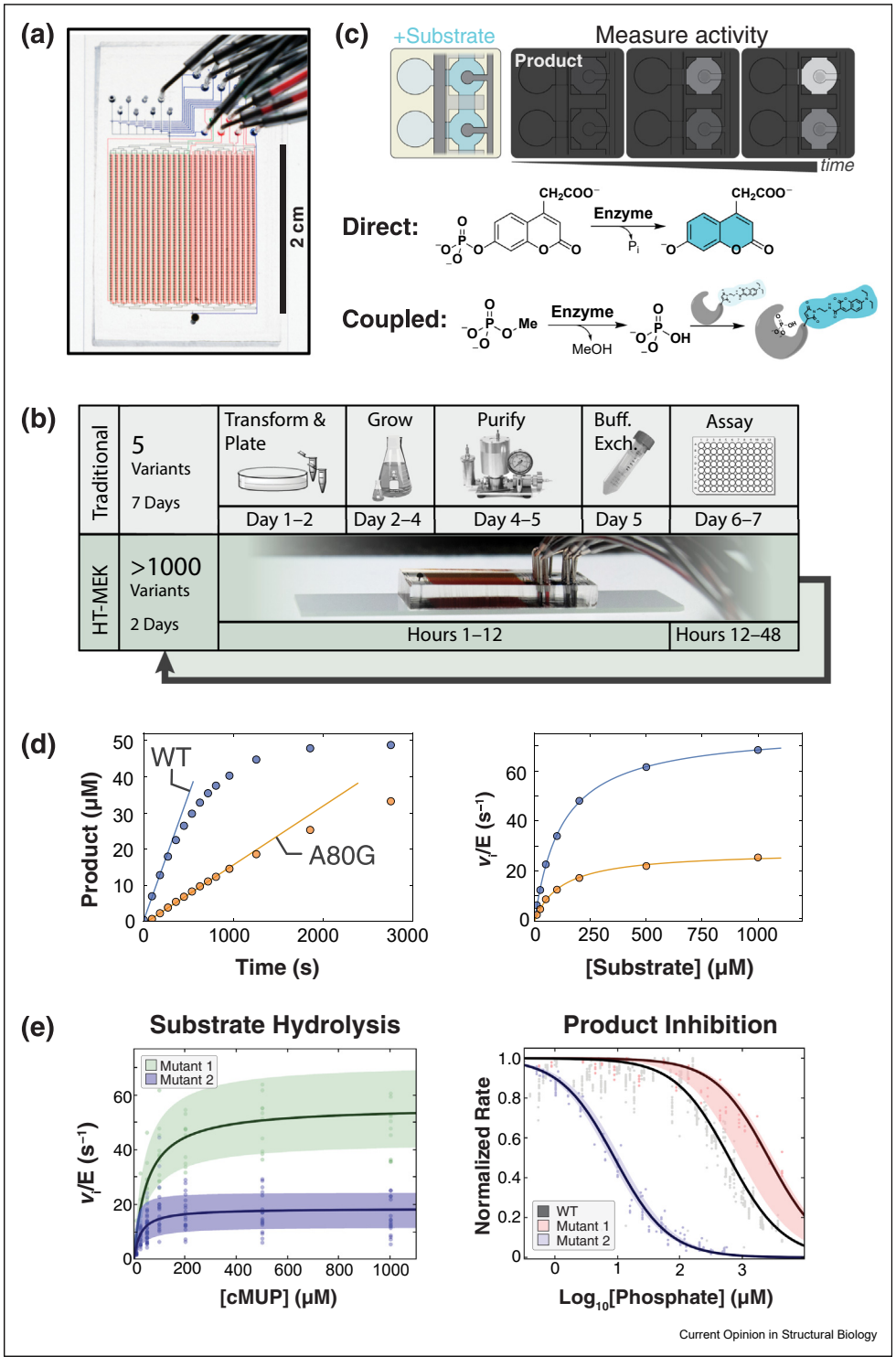

Application of HT-MEK to study catalysis and inhibition. (a) HT-MEK uses a valved microfluidic device containing >1500 chambers to **(b)** in vitro express, purify, and assay 1500 enzyme variants in days. Iteratively varying substrates, inhibitors, and conditions give kinetic and thermodynamic parameters of function. **(c)** Reactions are performed by introducing fluorogenic substrate (light blue) into reaction chambers and synchronously exposing surface-immobilized enzyme to the substrate with pneumatic valving. Product (darker blue) is quantified by fluorescence over time, using direct (fluorogenic) or indirect (coupled) assays. The assays shown are for phosphatase activity or for any enzyme that directly or indirectly generates inorganic phosphate. **(d)** Example on-chip fluorogenic substrate turnover curves for the PafA phosphatase with fit initial rates (left) and Michaelis–Menten curves (right) for wild type (blue, WT) and mutant (orange) PafA variants. A per chamber standard curve is used to convert fluorescence to product concentration. **(e)** Many replicates (within separate chambers) for each variant (Mutant 1: Y74V, Mutant 2: Y112G) over multiple chips are used to calculate bootstrap errors on fit Michaelis–Menten (left) and competitive inhibition (right) parameters (reproduced from Markin, Mokhtari, et al. (2021) [47]). HT-MEK, high-throughput microfluidic enzyme kinetics.

Consider, as an example, the active site arginine and lysine residues that contact one of the substrate phosphoryl oxygen atoms and are responsible for reaction specificity for phosphate monoesters over diesters (which are substrates of related superfamily members; [48–52]) (Figure 3b and c). Although mutation of most residues contacting these active site residues diminished specificity, a majority of the affecting residues were remote, including residues at the junction of three auxiliary domains (Figure 3d; auxiliary domains are structural regions present in subsets of Alkaline Phosphatase superfamily members [52]). The auxiliary domain junction sits ~20 Å from the active site and on the opposite side of the enzyme from the catalytic

Figure 3

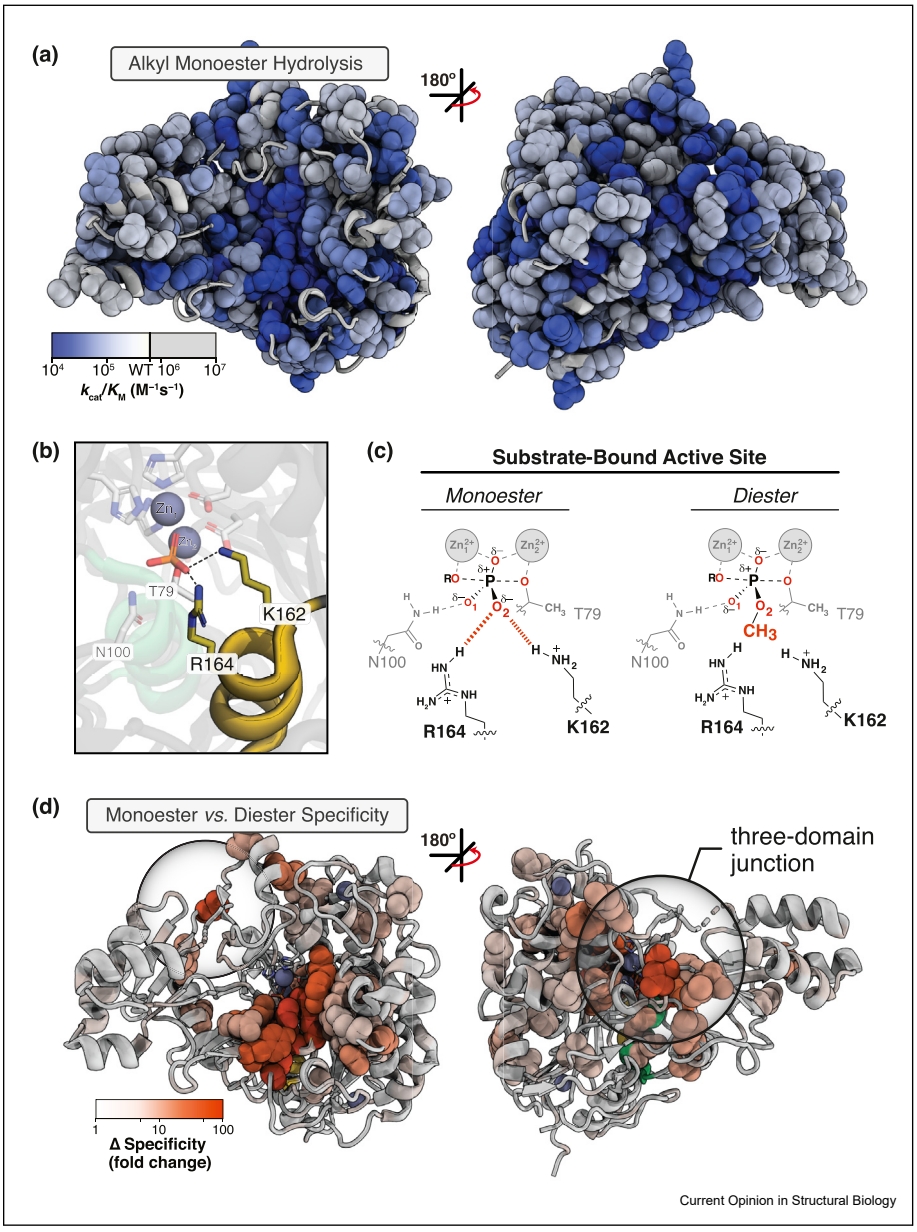

Spatial patterns of PafA mutational effects on specific functions. (a) Alkyl phosphate hydrolysis (k_{cat}/K_M) for glycine and valine substitutions at each position in PafA. Significant effects are shown as spheres, color-coded by the size of the effect. **(b)** The PafA-active site (PDBID: 5TJ3) showing contacts between covalently bound phosphate (T79) and active sites K162 and R164 (yellow sticks). **(c)** Schematic of PafA-active site residue contacts to bound phosphate monoester (left) versus diester (right) substrates. **(d)** Substrate specificity effects upon valine and glycine mutation of PafA positions, visualized as in **(a)**. Large mutational effects (spheres) cluster primarily around R164 and K162, extending distally to a three-domain junction (circled) more than 20 Å away. Panels **(a)**, **(c)**, and **(d)** are adapted from Markin, Mokhtari, et al. (2021) [47].

pocket but nevertheless exhibits mutational effects of up to 60-fold [47]. These observations suggest that the auxiliary domains and their positioning are critical for catalytic function by the active site arginine and lysine, but we would not have predicted these or other remote effects for mutations throughout PafA.

One would be tempted to conclude, in the absence of data to the contrary, that most distal functional effects arose from destabilizing the active enzyme. With HT-MEK (and related approaches under development), we can independently assay folding [47,53]. We found that none of the PafA effects arose from equilibrium unfolding (PafA is a secreted enzyme and is highly stable). Nevertheless, our ability to assay PafA with multiple substrates and under multiple expression and reaction conditions allowed us to uncover the presence of an unanticipated long-lived misfolded state of the enzyme. Without accounting for the effects of misfolding and unfolding on observed reaction rates, functional models cannot be unambiguously made or tested.

As noted previously, an immediate challenge is to predict distal effects for multiple enzymes and to use HT-MEK to determine what is correctly predicted, quantitatively or qualitatively. We can also directly use data from HT-MEK to aid enzyme engineering at a practical level. Functional maps generated by HT-MEK can inform where mutations should be made to enhance the chance of altering and tuning specific functional parameters. In addition, HT-MEK can rapidly assess human alleles to reveal the biophysical bases of mutations associated with disease and to inspire new and precise therapeutic strategies. For instance, the discovery of surface residues (through mutation) allosterically linked to function may allow druggable enzyme activation as well as inhibition [54].

Conformational ensembles for evaluating and building physical and catalytic models

Ultimately, we want to predict kinetic and thermodynamic constants for a particular reaction with a specified sequence. We can measure many of these values via HT-MEK as ground truths and compare them to values predicted by models, but these functional constants are emergent properties that result from the enzyme's underlying physical properties. We would like to have ground truths more closely connected to the enzyme's physical properties; these measurements would provide more direct tests to evaluate and improve physics-based models. In particular, we want to know an enzyme's conformational landscape and how this varies with bound ligands and through the enzyme's reaction, and we want to determine the affinities and reactivities of the states that constitute the landscape (Figure 1a–c).

The value of and need for ensemble information to understand protein folding and function have been recognized for decades [17,55,56]. For catalysis, the clear evidence for remote effects — from allosteric ligands and post-translational modifications — and efforts to understand how enzymes so efficiently navigate their reaction paths have led to a panoply of functional models that invoke dynamics (e.g. studies reported by Hammes et al., Schwartz, Hanoien et al., Kochen, and Warshel and Bora [57–61]). Experimentally, NMR provides relevant information about the rates of transitions between conformational states and information (e.g. order parameters) on the relative conformational freedom of residues (e.g. studies reported by Palmer and Alderson and Kay [62,63]). However, detailed atomic information that provides more direct tests of models, such as the extent and direction of motion and which motions are coupled or independent, is difficult to obtain via NMR. Fortunately, emerging X-ray crystallographic approaches can provide extensive and detailed information about conformational ensembles that can be more directly related to predictions from physics-based models.

A key technological breakthrough in X-ray crystallography was cryofreezing crystals to reduce their susceptibility to radiation damage and make crystal handling more reliable. Indeed, at least 90% of more than 150,000 protein X-ray structural models in the PDB were obtained under cryogenic conditions (diffraction source temperature $\leq$125 K) [25]. Nevertheless, X-ray structures can be obtained at ambient temperatures as well, conditions that do not quench a protein's inherent dynamic motions [64]. Ambient or 'room-temperature' (RT) X-ray crystallography requires high resolution (typically sub-1.5 Å) to provide reliable and extensive information about conformational heterogeneity at the atomic level and requires larger-than-average crystals to limit X-ray damage during data collection. Fortunately, many enzymes of interest yield crystals of the desired size and quality, and recent methodological improvements allow RT X-ray crystallography to be broadly implemented [65].

Conformational ensembles can also be generated from cryo X-ray structures, by combining multiple static structures into a so-called pseudoensemble [66,67]. In brief, it is assumed that individual cryogenic X-ray structures of proteins sharing the same or highly similar sequences (e.g. with one or a few mutations) provide conformers trapped in different low-energy wells on the protein's energy landscape, so that combining many cryo-structures can approximate the protein's accessible ensemble of states (for pseudoensemble computational tools, see studies reported by Monzon et al., Li et al., Zhang et al., and Grant et al. [68–71]). Although motions are restricted, and some are changed on freezing,

several lines of evidence and direct comparisons support a close correspondence of the flexibility within pseudoensembles and the motions present at ambient temperatures [67,72].

Pseudoensembles and RT data are complementary — the latter providing the most reliable information about conformational heterogeneity and the former retaining information about correlated motions within the constituent conformers. These approaches have provided insights into multiple systems, including HRas GTPase, protein tyrosine phosphatase, proline isomerase, soybean lipoxygenase, β-lactamase, dihydrofolate reductase, isocyanide hydratase, herpes virus protease, and designed and laboratory-evolved Kemp eliminases [73–83]. The most extensive X-ray ensemble data to be collected and analyzed is for ketosteroid isomerase (KSI; Figure 4a). For KSI, pseudoensembles and high-resolution RT ensembles have been obtained for complexes representing the states in the enzyme's reaction cycle, for KSIs from two different species, and for WT and mutant KSIs [72].

Figure 4

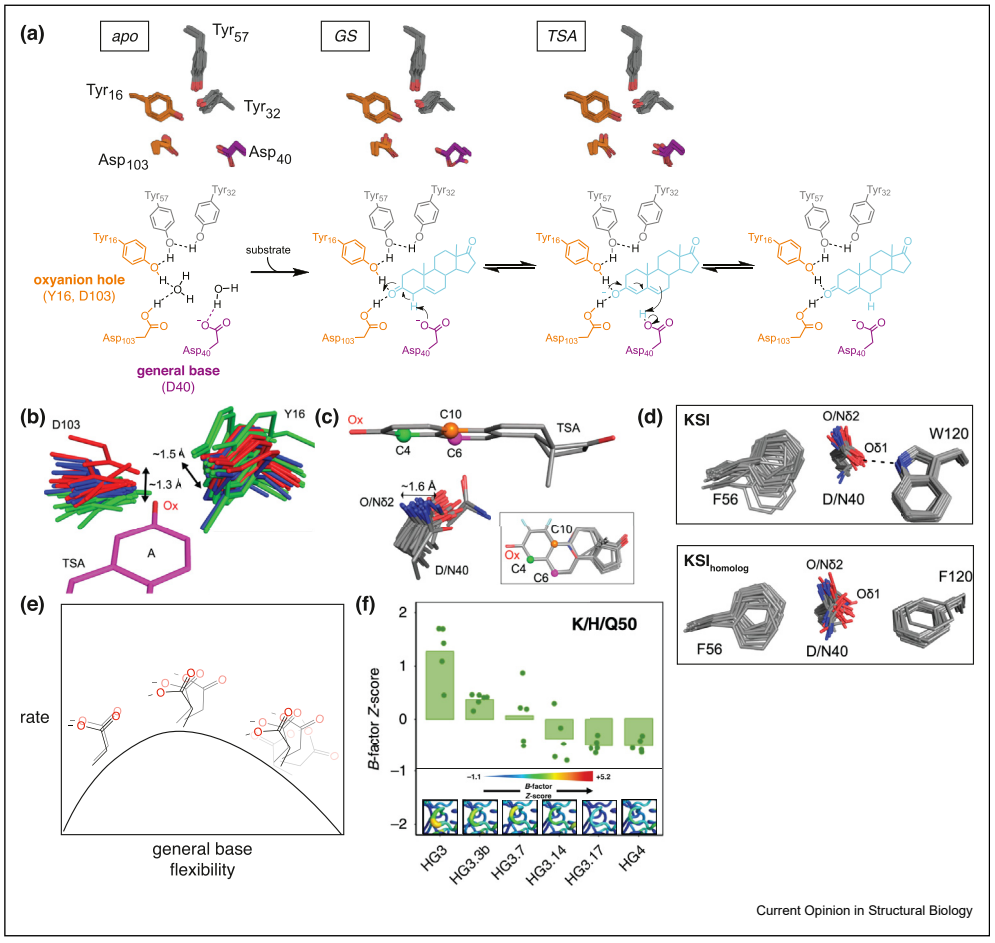

Ensemble crystallography provides mechanistic insights toward enzyme catalysis and engineering. (a) KSI reaction mechanism and ensemble crystallography of multiple states in the reaction cycle. Active-site residues from experimental RT multiconformer models are shown for apo, ground-state (GS) bound, and transition state analog (TSA) bound KSI. **(b, c)** Pseudoensembles for KSI oxyanion hole residues Y16 and D103 **(b)** and the general base (D40, wild type, or mutant D40N) **(c)**, derived from cryo-structures containing bound transition state analogs (TSA, equilenin and phenols). Bound TSAs were superimposed, aligned on phenol ('A') rings and shown as a single structure for simplicity. **(d)** Pseudoensemble for the KSI general base (D40 or mutant D40N) and neighboring residues for KSI (F56, W120) and a $KSI_{homolog}$ (F56, F120). KSI and $KSI_{homolog}$ k_{cat} measurements for both the WT and the position 120 reciprocal mutants (KSI W120F; $KSI_{homolog}$ F120W) demonstrate a 4-fold (KSI) and 8-fold ($KSI_{homolog}$) rate increase for phenylalanine versus tryptophan-containing variants. **(e)** Cartoon depiction of the relationship between KSI rate and general base (D40) flexibility. **(f)** Increase in active-site rigidity during directed evolution of a designed Kemp eliminase (from HG3 to HG4). B-factor Z-scores are plotted for each heavy atom of the position 50 side chain (K, H, or Q). Structural views of the Kemp eliminase residues 87–90 loop from room-temperature crystallography, with B-factor Z-scores colored as per legend and increasing with sausage plot thickness (inset). Panels **(b)** to **(e)** adapted from Yabukarski et al. (2020) [72]; panel **(f)** adapted with changes from Broom et al. [83] (http://creativecommons.org/licenses/by/4.0/). KI, ketosteroid isomerase; RT, room temperature.

Insights from KSI ensembles

The function of a catalytic residue depends not only on its presence in the vicinity of the substrate but also on the adoption of conformational states with the correct distance and orientation to the substrate and/or other residues. Indeed, positioning is universally invoked or assumed in descriptions of enzyme catalysis, but without ensemble information, we cannot know the nature and extent of this positioning. Ensemble information is also needed to understand the motion inherent in all chemical reactions, minimally to go from van der Waals distance to form a bond, a change on the order of 1 Å, and how or whether this is affected by the enzyme environment. Furthermore, many enzymes catalyze multistep reactions and use the same functional groups in different poses to carry out successive reaction steps. Again, ensemble information is needed to understand how enzymes navigate these challenges.

KSI, a steroid isomerase, abstracts a proton from its steroid substrate with a general base, transferring the proton to a different position of the resulting intermediate to give the more stable conjugated product, using an oxyanion hole to stabilize negative charge accumulation on the intermediate (Figure 4a). Oxyanion holes for serine proteases have been suggested to contribute catalytically via ground-state destabilization, by forming suboptimal, geometrically constrained hydrogen bonds that sit out of the plane of the ground state sp^2 oxygen [84–87]. The KSI ensembles reveal motions of the oxyanion hole hydrogen bond donors on the scale of ~1 Å and an absence of discrimination between the sp^2 and sp^3 oxygen electronic configurations (Figure 4b). Instead, the oxyanion hole seems to provide catalysis by forming hydrogen bonds that are stronger than those to water in solution [6,72,88–90].

Extensive site-directed mutagenesis studies revealed an astounding effective molarity of 10^3–10^5 M for the KSI aspartate general base [91]. Although the simplest explanation for this large catalytic effect is precise positioning, positioning at multiple sites would be required to accommodate KSI's multiple substrates and successive reaction steps. As previously mentioned, KSI ensembles allowed this model to be tested, revealing a broad distribution of general base positions (Figure 4c), as needed to abstract and donate protons at multiple positions and indicating that alternative models are needed to account for the highly efficient observed general base catalysis [91–93]. In addition, the flexibility in the oxyanion hole, while precluding ground-state destabilization, contributes to the conformational plasticity of the general base and substrate with respect to one another (Figure 4b and c).

One might expect there to be a balance between positioning and flexibility: clearly, too much flexibility of the KSI general base would hamper catalysis while too-restricted positioning could as well, by limiting access to the multiple states needed to carry out the full reaction cycle. Remarkably, functional results and ensembles for wild type and mutant KSIs provide evidence for the balance: an aromatic–anion interaction provides greater flexibility of the general base than a hydrogen bond and faster reaction, whereas mutations in the general base loop that disorder it substantially impair catalysis (Figure 4d and e).

In addition, comparisons of how conformational ensembles of KSI side chains change from mutations in nearby residues provide information about the balance of forces, including conformational entropy, that determine where and how much the oxyanion hole tyrosine is positioned [72] (Figure 4b). Effects such as these will provide rich testing grounds for force fields in physics-based models. Finally, the observation that, at least in this case, ensemble rearrangements remain local suggests at least some limitation to the complexity of models needed to account for energy landscapes of enzymes (Figure 1a and b; see also 'The complexity of functional models' in the following).

Rules for enzyme design from ensemble crystallography

A major challenge is to understand why the performance of de novo enzyme designs falls short of natural enzymes [94–96], and how to rationally engineer solutions that nature (or researchers) discover through evolution. Early de novo design of Kemp eliminases (KE) yielded some success [97], but the same fold rate enhancement, or more, for the eliminase reaction is achieved in the active site of KSI, an enzyme evolved to carry out different chemistry with different substrates. This result suggests that designed KEs accomplish only coarse positioning against a general base within a binding pocket [98]. With laboratory-evolved improvements (17 substitutions), a ~10^5-fold increase in k_{cat}/K_M was achieved [99]. Recent work from the Chica and Fraser groups sought to understand the mechanistic bases for these improvements, interrogating four variants along the mutational trajectory via RT crystallography [83,100]. This effort revealed that apo-state catalytic elements rigidified along the mutational trajectory, favoring catalytically preorganized poses, consistent with classical proposals for origins of catalysis from positioning of substrates and catalytic groups (Figure 4f) [93,101,102].

More generally, crystallographic ensembles can be used to test models of catalysis that attempt to link motions or positioning to function, identifying the types and scales of motions that may be relevant to progress along the reaction coordinate. This ability allows the structure–function paradigm to be supplanted by ensemble-function analyses.

Ensemble measurements versus the reaction coordinate

The X-ray ensemble approaches described previously are needed to relate structure to energetics and function but also have limitations. Most centrally, they provide information about the 'lower levels' of the enzyme's conformational landscape. States that are uphill by $>\sim 2$ kcal/mol, representing <5% of the total population, are unlikely to be observed. This limitation alone is not severe, as one can decipher much of the underlying energetics by having lots of data — as is provided by X-ray ensembles — in the $\sim 0-2$ kcal/mol energy range. But what is missing is information about the conformations and motions as one climbs further toward the reaction's transition state. Transition states are by definition fleeting states, lasting <1 ps, and highly improbable. To assess what happens at these rarified regions of the energy landscape and whether the data obtained closer to the base of these mountains are adequate to model the reaction coordinate, we need additional ground truths for these transient, high-energy states. Although such information cannot (yet) be obtained in high throughput, several methods exist to provide this critical information.

The highest time resolution structural data use laser pulses to initiate a process and serial high-resolution X-ray data collection. X-ray free-electron lasers and cutting-edge synchrotron sources capture crystallographic snapshots at ambient temperatures by supplying intense femtosecond X-ray pulses [103,104]. Tenboer et al. [105] used nanosecond laser pulses in conjunction with X-ray free-electron laser crystallography to isomerize the double bond of the photoactive yellow protein chromophore and to measure protein and chromophore conformational changes after time delays of 10 ns and 1 μs. These experiments revealed the significant side-chain displacements associated with photocycle transients at high resolution. Schlichting et al. [106] used a 150 fs laser pulse to dissociate CO from myoglobin and were able to follow in real-time the synchronous nonequilibrium picosecond oscillations of the heme ring that arise from the CO dissociation energy and dissipate on the order of 10—100 ps. Vibrational spectroscopy, although not directly measuring atomic positions, is particularly powerful because frequencies can be assigned to specific bonds located within proteins or bound reactants and can provide information about changes in the strength and properties of those interactions. Dyer and Callender [107] used temperature-jump infrared spectroscopy on the microsecond timescale to identify multiple distinct and noninterconverting substrate-binding conformations with different reactivities in lactate dehydrogenase, providing a detailed energetic map of reaction trajectories unavailable with traditional methods. It may also be possible to carry out time-resolved vibrational studies on enzyme libraries in high throughput. A critical next step will be to apply these synchronized approaches more broadly so that motions and transitions are not averaged among the population of molecules in the crystal [82].

The complexity of functional models

Residues are functionally, and thus energetically, interdependent. This interconnection is most simply appreciated by recognizing that without the 'right' residues surrounding the catalytic and binding residues those active site residues do not yield significant catalysis and vice versa [108]. Consequently, descriptions of 'residue function' cannot be made from single-mutant variants alone. The extent of residue connectivity — how many residues affect the function of a particular residue and by how much — defines the complexity of the model that is needed to mathematically describe an enzyme's function [109,110]. Although this complexity is likely to vary — for enzymes with different folds, with allostery, and so on — we want to know the scale and range of this complexity as it will dictate the form of models and how they are developed and tested [111,112].

We also know that residues are not fully interdependent (epistatic), as if this were the case any single mutation would shatter the active site and fully abolish activity. Classical mutational studies have found some regions, including active sites, with limited energetic dependencies among sets of three or fewer residues [113—115]. In one striking case, a single residue change was predominantly responsible for improved activity in psychrophiles versus improved stability in thermophiles [116]. Phylogenetic comparisons, verified experimentally, identified two nearby residue changes needed to fully shift stability and activity but with much smaller effects.

Phylogenetic comparisons across many enzyme families containing psychrophilic, mesophilic, and thermophilic variants suggested instances of limited epistasis in temperature adaptation [116]. Most of these covarying sets of residues corresponded primarily to pairs of residues that correlate with temperature adaptation and likely confer function within divergent sequence backgrounds of a given enzyme family. These observations suggest substantial simplifications in residue interdependences and model complexity in many cases. Nevertheless, there are also larger co-occurring sets, and our initial HT-MEK experiments in PafA have also identified functional interconnections among tens of residues in regions extending from the active site to the surface.

Experimentally, even measuring effects of all possible triple-mutant substitutions within a single small (100 residue) enzyme is intractable as it would require $>10^9$ variants. Instead, it will be necessary to prioritize higher-order mutants most likely to be informative, guided by

maps of enzyme architecture identified in initial HT-MEK surveys and additional phylogenetic information such as that described to understand temperature adaptation [117]. This is an area that will likely require innovative ideas and rigorous tests to identify paths toward predictive models. The lengths of those paths and the difficulty in traversing them will be determined by how rapidly partially predictive physics-based models can be developed and used as guides.

Conclusion and outlook

Accurate quantitative prediction of protein and enzyme functions from amino acid sequence is the ultimate litmus test of our biophysical understanding. But as other disciplines have experienced, breakthroughs frequently arrive later than hoped, and only with sustained effort at the nexus of a deep need, technological development, and an empirical or theoretical framework.

The need for accurate and general quantitative models of functional prediction is clear — they would transform medicine, industry, and biotechnology. But what remains uncertain is whether we possess the requisite theoretical and technological foundation. Where we stand is likely to be clarified only through careful tests of current general predictive models and algorithms, particularly physics-based ones, using blinded comparisons to large-scale empirical measurements. With HT-MEK and crystallographic ensembles, we are starting to acquire the needed quality and quantity of data to compare with predictions.

Most immediately, HT-MEK can be used to study new enzymes, as it can be applied to any enzyme with a direct or coupled fluorogenic assay. HT-MEK, and extensions to it currently under development, can assay protein stability as well as function, and important applications include dissecting the functional effects of human alleles that do or may cause disease; providing foundational information to guide protein engineering and design efforts using current approaches; and combining enzymes to efficiently engineer metabolic pathways.

We envision a future wherein large-scale mutational studies are routinely performed with HT-MEK. In this future, analysis, interpretation, and modeling are the rate-limiting steps of advancing protein biochemistry, instead of experimentation. To drive future advances in these models, conformational ensembles will provide ground-truth atomic positions and motions and describe how these are altered in mutants of differing functions. Ensembles can be assembled for many enzymes from the vast data available in the PDB [72], and ensemble information can now be readily attained for new enzyme complexes and variants through advances in room temperature data collection [65].

We suspect that a 'critical assessment of quantitative protein function' will be needed. Although blind protein function prediction challenges exist, these contests typically use in vivo coarse phenotypic data (e.g. whether or not particular mutations are deleterious) as targets, reflecting the absence of and need for large-scale in vitro quantitative measurements of specific functional parameters [118,119]. A new effort would involve solicitation of large-scale quantitative functional data sets ahead of publication and creation of objective metrics for success that scale across different parameters and sizes of data sets. We look forward to contributing to this effort by basic scientists, engineers, and theoreticians.

Finally, with deep functional data in hand, it will also be possible to extend predictive models to the systems level, connecting the basic enzyme properties responsible for selective advantages observed in DMS experiments and in natural and laboratory evolution. Here, comparisons of effects predicted from metabolic models for particular kinetic perturbations with experimental measurements of fitness and of metabolite levels will provide a path to develop robust models to understand cellular metabolism and to engineer new metabolic pathways.

Conflict of interest statement

Nothing declared.

Acknowledgements

The authors dedicate this article to the memory of Dan Tawfik who recently and tragically passed away. Dan's creativity and enthusiasm was an inspiration to us and many others. The authors thank Craig Markin, Siyuan Du, and members of the Herschlag and Fordyce laboratories for helpful discussions and review. This work was supported with funding from the National Institutes of Health (NIH) R01 grant (GM064798), the Gordon and Betty Moore Foundation grant, and the Ono Pharma Foundation Breakthrough Initiative Prize awarded to D.H. and P.M.F and the National Science Foundation (NSF) grant (MCB-1714723) awarded to D.H. D.A.M. acknowledges support from the Stanford Medical Scientist Training Program and the Stanford Interdisciplinary Graduate Fellowship (Anonymous Donor) affiliated with Stanford ChEM-H. P.M.F. is a Chan Zuckerberg Biohub investigator.

References

Papers of particular interest, published within the period of review, have been highlighted as:

- • of special interest
- •• of outstanding interest

1. **CASP13 proceedings**. *Proteins* 2019, **87**:1007–1388.
2. Senior AW, Evans R, Jumper J, Kirkpatrick J, Sifre L, Green T, Qin C, Žídek A, Nelson AWR, Bridgland A, *et al.*: **Improved protein structure prediction using potentials from deep learning**. *Nature* 2020, **577**:706–710.
3. Kato Y, Miyakawa T, Tanokura M: **Overview of the mechanism of cytoskeletal motors based on structure**. *Biophys Rev* 2018, **10**:571–581.
4. Indiani C, O'Donnell M: **The replication clamp-loading machine at work in the three domains of life**. *Nat Rev Mol Cell Biol* 2006, **7**:751–761.

5. Keskin O, Nussinov R: **Favorable scaffolds: proteins with different sequence, structure and function may associate in similar ways**. *Protein Eng Des Sel* 2005, **18**:11–24.

6. Kraut DA, Sigala PA, Pybus B, Liu CW, Ringe D, Petsko GA, Herschlag D: **Testing electrostatic complementarity in enzyme catalysis: hydrogen bonding in the Ketosteroid Isomerase oxyanion hole**. *PLoS Biol* 2006, **4**:e99.

7. Lee J, Goodey NM: **Catalytic contributions from remote regions of enzyme structure**. *Chem Rev* 2011, **111**:7595–7624.

8. Hilser VJ, Wrabl JO, Motlagh HN: **Structural and energetic basis of allostery**. *Annu Rev Biophys* 2012, **41**:585–609.

9. Nussinov R, Tsai C-J: **Allostery in disease and in drug discovery**. *Cell* 2013, **153**:293–305.

10. Reynolds KA, McLaughlin RN, Ranganathan R: **Hot spots for allosteric regulation on protein surfaces**. *Cell* 2011, **147**:1564–1575.

11. Wrenbeck EE, Azouz LR, Whitehead TA: **Single-mutation fitness landscapes for an enzyme on multiple substrates reveal specificity is globally encoded**. *Nat Commun* 2017, **8**:15695.

12. Lee J, Natarajan M, Nashine VC, Socolich M, Vo T, Russ WP, Benkovic SJ, Ranganathan R: **Surface sites for engineering allosteric control in proteins**. *Science* 2008, **322**:438.

13. Dryden DTF, Thomson AR, White JH: **How much of protein sequence space has been explored by life on Earth?** *J R Soc Interface* 2008, **5**:953–956.

14. Marks DS, Colwell LJ, Sheridan R, Hopf TA, Pagnani A, Zecchina R, Sander C: **Protein 3D structure computed from evolutionary sequence variation**. *PloS One* 2011, **6**:e28766.

15. Lau KF, Dill KA: **A lattice statistical mechanics model of the conformational and sequence spaces of proteins**. *Macromolecules* 1989, **22**:3986–3997.

16. Adcock SA, McCammon JA: **Molecular dynamics: survey of methods for simulating the activity of proteins**. *Chem Rev* 2006, **106**:1589–1615.

17. Frauenfelder H, Sligar S, Wolynes P: **The energy landscapes and motions of proteins**. *Science* 1991, **254**:1598–1603.

18. Wei G, Xi W, Nussinov R, Ma B: **Protein ensembles: how does nature harness thermodynamic fluctuations for life? The diverse functional roles of conformational ensembles in the cell**. *Chem Rev* 2016, **116**:6516–6551.

19. Aesop Gibbs L. *Aesop's fables*. Oxford University Press; 2008.

20. Claeyssens F, Harvey JN, Manby FR, Mata RA, Mulholland AJ, Ranaghan KE, Schütz M, Thiel S, Thiel W, Werner H-J: **High-accuracy computation of reaction barriers in enzymes**. *Angew Chem Int Ed* 2006, **45**:6856–6859.

21. Mulholland AJ: **Chemical accuracy in QM/MM calculations on enzyme-catalysed reactions**. *Chem Cent J* 2007, **1**:19.

22. Stevenson Angus. In *Christine A. Lindberg: new oxford American dictionary*. 3 ed. Oxford University Press; 2010.

23. Wooley JC, Ye Y: **A historical perspective and overview of protein structure prediction**. In *Computational methods for protein structure prediction and modeling*. Edited by Xu Y, Xu D, Liang J, New York: Springer; 2007:1–43.

24. Moult J, Fidelis K, Kryshtafovych A, Schwede T, Tramontano A: **Critical assessment of methods of protein structure prediction (CASP) - round x: critical assessment of structure prediction**. *Proteins* 2014, **82**:1–6.

25. Berman HM: **The protein Data Bank**. *Nucleic Acids Res* 2000, **28**:235–242.

26. Das R, Baker D: **Macromolecular modeling with Rosetta**. *Annu Rev Biochem* 2008, **77**:363–382.

27. Kamisetty H, Ovchinnikov S, Baker D: **Assessing the utility of coevolution-based residue-residue contact predictions in a sequence- and structure-rich era**. *Proc Natl Acad Sci U S A* 2013, **110**:15674–15679.

28. AlQuraishi M: **End-to-end differentiable learning of protein structure**. *Cell Systems* 2019, **8**:292–301.

29. Kuhlman B, Bradley P: **Advances in protein structure prediction and design**. *Nat Rev Mol Cell Biol* 2019, **20**:681–697.

30. Alford RF, Leaver-Fay A, Jeliazkov JR, O'Meara MJ, DiMaio FP, Park H, Shapovalov MV, Renfrew PD, Mulligan VK, Kappel K, *et al.*: **The Rosetta all-atom energy function for macromolecular modeling and design**. *J Chem Theor Comput* 2017, **13**:3031–3048.

31. Fowler DM, Fields S: **Deep mutational scanning: a new style of protein science**. *Nat Methods* 2014, **11**:801–807.

32. Esposito D, Weile J, Shendure J, Starita LM, Papenfuss AT, Roth FP, Fowler DM, Rubin AF: **MaveDB: an open-source platform to distribute and interpret data from multiplexed assays of variant effect**. *Genome Biol* 2019, **20**:223.

33. Starr TN, Thornton JW: **Epistasis in protein evolution: epistasis in protein evolution**. *Protein Sci* 2016, **25**:1204–1218.

34. •• Mehlhoff JD, Stearns FW, Rohm D, Wang B, Tsou E-Y, Dutta N, Hsiao M-H, Gonzalez CE, Rubin AF, Ostermeier M: **Collateral fitness effects of mutations**. *Proc Natl Acad Sci U S A* 2020, **117**:11597–11607.

Cellular fitness effects of mutations in protein-coding genes can arise from defects unrelated to the gene's specific function, like misfolding, aggregation, and stress induction. The authors found that for TEM-1 β-lactamase, these "collateral" mutational effects can occur as often or more than effects on intrinsic function or abundance, suggesting fitness-based deep mutational scanning data can reflect phenotypes with limited linkage to specific function.

35. Romero PA, Tran TM, Abate AR: **Dissecting enzyme function with microfluidic-based deep mutational scanning**. *Proc Natl Acad Sci U S A* 2015, **112**:7159–7164.

36. Harris DT, Wang N, Riley TP, Anderson SD, Singh NK, Procko E, Baker BM, Kranz DM: **Deep mutational scans as a guide to engineering high affinity T cell receptor interactions with peptide-bound major histocompatibility complex**. *J Biol Chem* 2016, **291**:24566–24578.

37. Bandaru P, Shah NH, Bhattacharyya M, Barton JP, Kondo Y, Cofsky JC, Gee CL, Chakraborty AK, Kortemme T, Ranganathan R, *et al.*: **Deconstruction of the Ras switching cycle through saturation mutagenesis**. *eLife* 2017, **6**:e27810.

38. Tamer YT, Gaszek IK, Abdizadeh H, Batur T, Reynolds K, Atilgan AR, Atilgan C, Toprak E: **High-order epistasis in catalytic power of dihydrofolate reductase gives rise to a rugged fitness landscape in the presence of trimethoprim selection**. *Mol Biol Evol* 2019, **36**:1533–1550.

39. •• Thompson S, Zhang Y, Ingle C, Reynolds KA, Kortemme T: **Altered expression of a quality control protease in E. coli reshapes the in vivo mutational landscape of a model enzyme**. *eLife* 2020, **9**:e53476.

Examined the impacts of altered cellular contexts on the mutational sensitivity of DHFR using deep mutational scanning. The authors observed that presence or absence of cellular quality control machinery (Lon protease) substantially altered mutational effects with cell fitness as a readout, and that apparently advantageous variants become deleterious when Lon was present. These findings suggest widespread activity–stability tradeoffs that can be masked or elicited depending on the specific strains and conditions used when performing deep mutational scanning.

40. Baase WA, Liu L, Tronrud DE, Matthews BW: **Lessons from the lysozyme of phage T4**. *Protein Sci* 2010, **19**:631–641.

41. Tang Q, Fenton AW: **Whole-protein alanine-scanning mutagenesis of allostery: a large percentage of a protein can contribute to mechanism**. *Hum Mutat* 2017, **38**:1132–1143.

42. Carlin DA, Caster RW, Wang X, Betzenderfer SA, Chen CX, Duong VM, Ryklansky CV, Alpekin A, Beaumont N, Kapoor H, *et al.*: **Kinetic characterization of 100 glycoside hydrolase mutants enables the discovery of structural features correlated with kinetic constants**. *PloS One* 2016, **11**, e0147596.

43. Carlin DA, Hapig-Ward S, Chan BW, Damrau N, Riley M, Caster RW, Bethards B, Siegel JB: **Thermal stability and kinetic constants for 129 variants of a family 1 glycoside hydrolase**

reveal that enzyme activity and stability can be separately designed. *PloS One* 2017, **12**, e0176255.

44. Maerkl SJ, Quake SR: **A systems approach to measuring the binding energy landscapes of transcription factors**. *Science* 2007, **315**:233–237.

45. Fordyce PM, Gerber D, Tran D, Zheng J, Li H, DeRisi JL, Quake SR: **De novo identification and biophysical characterization of transcription-factor binding sites with microfluidic affinity analysis**. *Nat Biotechnol* 2010, **28**:970–975.

46. Aditham AK, Markin CJ, Mokhtari DA, DelRosso N, Fordyce PM: **High-throughput affinity measurements of transcription factor and DNA Mutations reveal affinity and specificity determinants**. *Cell Syst* 2021, **12**:112–127. e11.

47. •• Markin CJ, Mokhtari DA, Sunden F, Appel MJ, Akiva E, Longwell SA, Sabatti C, Herschlag D, Fordyce PM: **Revealing enzyme functional architecture via high-throughput microfluidic enzyme kinetics**. *Science* 2021, **373**(6553), eabf8761, https://doi.org/10.1101/2020.11.24.383182.
Development and application of a high-throughput platform for simultaneous protein expression, purification, and kinetic analysis for 1500 enzyme variants. This study revealed enzyme functional architecture by obtaining and comparing multiple catalytic and binding parameters for mutations at every position of a highly-proficient phosphate monoesterase.

48. Sunden F, AlSadhan I, Lyubimov AY, Ressl S, Wiersma-Koch H, Borland J, Brown CL, Johnson TA, Singh Z, Herschlag D: **Mechanistic and evolutionary insights from comparative enzymology of phosphomonoesterases and phosphodiesterases across the alkaline phosphatase superfamily**. *J Am Chem Soc* 2016, **138**:14273–14287.

49. O'Brien PJ, Herschlag D: **Functional interrelationships in the alkaline phosphatase superfamily: phosphodiesterase activity of Escherichia coli alkaline phosphatase**. *Biochemistry* 2001, **40**:5691–5699.

50. Zalatan JG, Fenn TD, Brunger AT, Herschlag D: **Structural and functional comparisons of Nucleotide Pyrophosphatase/Phosphodiesterase and Alkaline Phosphatase: implications for mechanism and evolution**. *Biochemistry* 2006, **45**:9788–9803.

51. Wiersma-Koch H, Sunden F, Herschlag D: **Site-directed mutagenesis maps interactions that enhance cognate and limit promiscuous catalysis by an alkaline phosphatase superfamily phosphodiesterase**. *Biochemistry* 2013, **52**:9167–9176.

52. Sunden F, AlSadhan I, Lyubimov A, Doukov T, Swan J, Herschlag D: **Differential catalytic promiscuity of the alkaline phosphatase superfamily bimetallo core reveals mechanistic features underlying enzyme evolution**. *J Biol Chem* 2017, **292**:20960–20974.

53. Atsavapranee B, Stark CD, Sunden F, Thompson S, Fordyce PM: **Fundamentals to function: quantitative and scalable approaches for measuring protein stability**. *Cell Systems* 2021, **12**(6):547–560.

54. Abdel-Magid AF: **Allosteric modulators: an emerging concept in drug discovery**. *ACS Med Chem Lett* 2015, **6**:104–107.

55. Frauenfelder H, Petsko GA, Tsernoglou D: **Temperature-dependent X-ray diffraction as a probe of protein structural dynamics**. *Nature* 1979, **280**:558–563.

56. Hartmann H, Parak F, Steigemann W, Petsko GA, Ponzi DR, Frauenfelder H: **Conformational substates in a protein: structure and dynamics of metmyoglobin at 80 K**. *Proc Natl Acad Sci U S A* 1982, **79**:4967–4971.

57. Hammes GG, Benkovic SJ, Hammes-Schiffer S: **Flexibility, diversity, and cooperativity: pillars of enzyme catalysis**. *Biochemistry* 2011, **50**:10422–10430.

58. Schwartz SD: **Protein dynamics and the enzymatic reaction coordinate**. In *Dynamics in enzyme catalysis*. Edited by Klinman J, Hammes- Schiffer S, Berlin Heidelberg: Springer; 2013:189–208.

59. Hanoian P, Liu CT, Hammes-Schiffer S, Benkovic S: **Perspectives on electrostatics and conformational motions in enzyme catalysis**. *Acc Chem Res* 2015, **48**:482–489.

60. Kohen A: **Role of dynamics in enzyme catalysis: substantial versus semantic controversies**. *Acc Chem Res* 2015, **48**:466–473.

61. Warshel A, Bora RP: **Perspective: defining and quantifying the role of dynamics in enzyme catalysis**. *J Chem Phys* 2016, **144**:180901.

62. Palmer AG: **NMR characterization of the dynamics of biomacromolecules**. *Chem Rev* 2004, **104**:3623–3640.

63. Alderson TR, Kay LE: **NMR spectroscopy captures the essential role of dynamics in regulating biomolecular function**. *Cell* 2021, **184**:577–595.

64. Halle B: **Biomolecular cryocrystallography: structural changes during flash-cooling**. *Proc Natl Acad Sci U S A* 2004, **101**:4793–4798.

65. • Doukov T, Herschlag D, Yabukarski F: **Instrumentation and experimental procedures for robust collection of X-ray diffraction data from protein crystals across physiological temperatures**. *J Appl Crystallogr* 2020, **53**:1493–1501.
Reports experimental strategies to facilitate the collection of high resolution (<1.5 Å) x-ray structures at above-room temperatures, up to 363 K. Applied to proteinase K, thaumatin, and lysozyme crystals, this approach is generalizable to crystallographic study of other enzymes at physiological temperatures and can be readily implemented at other beamlines.

66. Zoete V, Michielin O, Karplus M: **Relation between sequence and structure of HIV-1 protease inhibitor complexes: a model system for the analysis of protein flexibility**. *J Mol Biol* 2002, **315**:21–52.

67. Best RB, Lindorff-Larsen K, DePristo MA, Vendruscolo M: **Relation between native ensembles and experimental structures of proteins**. *Proc Natl Acad Sci U S A* 2006, **103**:10901–10906.

68. Monzon AM, Rohr CO, Fornasari MS, Parisi G: **CoDNaS 2.0: a comprehensive database of protein conformational diversity in the native state**. *Database* 2016, **2016**, baw038.

69. Li Z, Jaroszewski L, Iyer M, Sedova M, Godzik A: **Fatcat 2.0: towards a better understanding of the structural diversity of proteins**. *Nucleic Acids Res* 2020, **48**:W60–W64.

70. Zhang S, Krieger JM, Zhang Y, Kaya C, Kaynak B, Mikulska-Ruminska K, Doruker P, Li H, Bahar I: **ProDy 2.0: increased scale and scope after 10 years of protein dynamics modelling with Python**. *Bioinformatics* 2021:btab187, https://doi.org/10.1093/bioinformatics/btab187.

71. Grant BJ, Skjærven L, Yao X: **The Bio3D packages for structural bioinformatics**. *Protein Sci* 2021, **30**:20–30.

72. •• Yabukarski F, Biel JT, Pinney MM, Doukov T, Powers AS, Fraser JS, Herschlag D: **Assessment of enzyme active site positioning and tests of catalytic mechanisms through X-ray–derived conformational ensembles**. *Proc Natl Acad Sci U S A* 2020, **117**:33204–33215.
Obtains conformational ensembles from "room temperature" cryogenic X-ray diffraction data for wild type and mutant ketosteroid isomerase in complexes representative of the states through its reaction cycle. Ensemble-function analysis is applied to evaluate catalytic models and the forces underlying positioning of active site residues.

73. Fraser JS, Clarkson MW, Degnan SC, Erion R, Kern D, Alber T: **Hidden alternative structures of proline isomerase essential for catalysis**. *Nature* 2009, **462**:669–673.

74. Fraser JS, van den Bedem H, Samelson AJ, Lang PT, Holton JM, Echols N, Alber T: **Accessing protein conformational ensembles using room-temperature X-ray crystallography**. *Proc Natl Acad Sci U S A* 2011, **108**:16247–16252.

75. Keedy DA, van den Bedem H, Sivak DA, Petsko GA, Ringe D, Wilson MA, Fraser JS: **Crystal cryocooling distorts conformational heterogeneity in a model Michaelis complex of DHFR**. *Structure* 2014, **22**:899–910.

76. Dellus-Gur E, Elias M, Caselli E, Prati F, Salverda MLM, de Visser JAGM, Fraser JS, Tawfik DS: **Negative epistasis and evolvability in TEM-1 β-Lactamase—the thin line between an enzyme's conformational freedom and disorder**. *J Mol Biol* 2015, **427**:2396–2409.

77. Keedy DA, Kenner LR, Warkentin M, Woldeyes RA, Hopkins JB, Thompson MC, Brewster AS, Van Benschoten AH, Baxter EL, Uervirojnangkoorn M, *et al.*: **Mapping the conformational landscape of a dynamic enzyme by multitemperature and XFEL crystallography**. *eLife* 2015, **4**, e07574.

78. Acker TM, Gable JE, Bohn M-F, Jaishankar P, Thompson MC, Fraser JS, Renslo AR, Craik CS: **Allosteric inhibitors, crystallography, and comparative analysis reveal network of coordinated movement across human herpesvirus proteases**. *J Am Chem Soc* 2017, **139**:11650–11653.

79. Offenbacher AR, Hu S, Poss EM, Carr CAM, Scouras AD, Prigozhin DM, Iavarone AT, Palla A, Alber T, Fraser JS, *et al.*: **Hydrogen–deuterium exchange of lipoxygenase uncovers a relationship between distal, solvent exposed protein motions and the thermal activation barrier for catalytic proton-coupled electron tunneling**. *ACS Cent Sci* 2017, **3**:570–579.

80. Keedy DA, Hill ZB, Biel JT, Kang E, Rettenmaier TJ, Brandão-Neto J, Pearce NM, von Delft F, Wells JA, Fraser JS: **An expanded allosteric network in PTP1B by multitemperature crystallography, fragment screening, and covalent tethering**. *eLife* 2018, **7**:e36307.

81. • Hu S, Offenbacher AR, Thompson EM, Gee CL, Wilcoxen J, Carr CAM, Prigozhin DM, Yang V, Alber T, Britt RD, *et al.*: **Biophysical characterization of a disabled double mutant of soybean lipoxygenase: the "undoing" of precise substrate positioning relative to metal cofactor and an identified dynamical network**. *J Am Chem Soc* 2019, **141**:1555–1567.
Reports room-temperature crystallography, EPR and hydrogen-deuterium exchange for soybean lipoxygenase. By comparing ensembles of WT and active site mutants, the authors identified an altered microenvironment (motions and interactions) around the iron cofactor that impairs optimal substrate binding for hydrogen transfer.

82. Dasgupta M, Budday D, de Oliveira SHP, Madzelan P, Marchany-Rivera D, Seravalli J, Hayes B, Sierra RG, Boutet S, Hunter MS, *et al.*: **Mix-and-inject XFEL crystallography reveals gated conformational dynamics during enzyme catalysis**. *Proc Natl Acad Sci U S A* 2019, **116**:25634–25640.

83. •• Broom A, Rakotoharisoa RV, Thompson MC, Zarifi N, Nguyen E, Mukhametzhanov N, Liu L, Fraser JS, Chica RA: **Ensemble-based enzyme design can recapitulate the effects of laboratory directed evolution in silico**. *Nat Commun* 2020, **11**:4808.
Determines the mechanistic basis for catalytic improvements provided by directed evolution of a de novo designed Kemp eliminase. Ensemble crystallography was used to identify more favorable positioning of active site residues along the mutational trajectory of evolved variants.

84. Robertus JD, Kraut J, Alden RA, Birktoft JJ: **Subtilisin. Stereochemical mechanism involving transition-state stabilization**. *Biochemistry* 1972, **11**:4293–4303.

85. Kraut J: **Serine proteases: structure and mechanism of catalysis**. *Annu Rev Biochem* 1977, **46**:331–358.

86. Kamerlin SCL, Chu ZT, Warshel A: **On catalytic preorganization in oxyanion holes: highlighting the problems with the gas-phase modeling of oxyanion holes and illustrating the need for complete enzyme models**. *J Org Chem* 2010, **75**:6391–6401.

87. Simón L, Goodman JM: **Hydrogen-bond stabilization in oxyanion holes: grand jeté to three dimensions**. *Org Biomol Chem* 2012, **10**:1905.

88. Sigala PA, Kraut DA, Caaveiro JMM, Pybus B, Ruben EA, Ringe D, Petsko GA, Herschlag D: **Testing geometrical discrimination within an enzyme active site: constrained hydrogen bonding in the ketosteroid isomerase oxyanion hole**. *J Am Chem Soc* 2008, **130**:13696–13708.

89. Sigala PA, Fafarman AT, Schwans JP, Fried SD, Fenn TD, Caaveiro JMM, Pybus B, Ringe D, Petsko GA, Boxer SG, *et al.*: **Quantitative dissection of hydrogen bond-mediated proton transfer in the ketosteroid isomerase active site**. *Proc Natl Acad Sci U S A* 2013, **110**:E2552–E2561.

90. Pinney MM, Natarajan A, Yabukarski F, Sanchez DM, Liu F, Liang R, Doukov T, Schwans JP, Martinez TJ, Herschlag D: **Structural coupling throughout the active site hydrogen bond networks of Ketosteroid Isomerase and Photoactive Yellow Protein**. *J Am Chem Soc* 2018, **140**:9827–9843.

91. Lamba V, Yabukarski F, Pinney M, Herschlag D: **Evaluation of the catalytic contribution from a positioned general base in Ketosteroid Isomerase**. *J Am Chem Soc* 2016, **138**:9902–9909.

92. Jindal G, Warshel A: **Misunderstanding the preorganization concept can lead to confusions about the origin of enzyme catalysis**. *Proteins* 2017, **85**:2157–2161.

93. Menger FM, Nome F: **Interaction vs preorganization in enzyme catalysis. A dispute that calls for resolution**. *ACS Chem Biol* 2019, **14**:1386–1392.

94. Lassila JK, Baker D, Herschlag D: **Origins of catalysis by computationally designed retroaldolase enzymes**. *Proc Natl Acad Sci U S A* 2010, **107**:4937–4942.

95. Hilvert D: **Design of protein catalysts**. *Annu Rev Biochem* 2013, **82**:447–470.

96. Kiss G, Çelebi-Ölçüm N, Moretti R, Baker D, Houk KN: **Computational enzyme design**. *Angew Chem Int Ed* 2013, **52**:5700–5725.

97. Röthlisberger D, Khersonsky O, Wollacott AM, Jiang L, DeChancie J, Betker J, Gallaher JL, Althoff EA, Zanghellini A, Dym O, *et al.*: **Kemp elimination catalysts by computational enzyme design**. *Nature* 2008, **453**:190–195.

98. Lamba V, Sanchez E, Fanning LR, Howe K, Alvarez MA, Herschlag D, Forconi M: **Kemp eliminase activity of ketosteroid isomerase**. *Biochemistry* 2017, **56**:582–591.

99. Blomberg R, Kries H, Pinkas DM, Mittl PR, Grutter MG, Privett HK, Mayo SL, Hilvert D: **Precision is essential for efficient catalysis in an evolved Kemp eliminase**. *Nature* 2013, **503**:418–421.

100. Otten R, Pádua RAP, Bunzel HA, Nguyen V, Pitsawong W, Patterson M, Sui S, Perry SL, Cohen AE, Hilvert D, *et al.*: **How directed evolution reshapes the energy landscape in an enzyme to boost catalysis**. *Science* 2020, **307**:1442–1446, https://doi.org/10.1126/science.abd3623.

101. Page MI, Jencks WP: **Entropic contributions to rate accelerations in enzymic and intramolecular reactions and the chelate effect**. *Proc Natl Acad Sci U S A* 1971, **68**:1678–1683.

102. Menger FM: **On the source of intramolecular and enzymatic reactivity**. *Acc Chem Res* 1985, **18**:128–134.

103. Chapman HN: **X-ray free-electron lasers for the structure and dynamics of macromolecules**. *Annu Rev Biochem* 2019, **88**:35–58.

104. Orville AM: **Recent results in time resolved serial femtosecond crystallography at XFELs**. *Curr Opin Struct Biol* 2020, **65**:193–208.

105. Tenboer J, Basu S, Zatsepin N, Pande K, Milathianaki D, Frank M, Hunter M, Boutet S, Williams GJ, Koglin JE, *et al.*: **Time-resolved serial crystallography captures high-resolution intermediates of photoactive yellow protein**. *Science* 2014, **346**:1242–1246.

106. Barends TRM, Foucar L, Ardevol A, Nass K, Aquila A, Botha S, Doak RB, Falahati K, Hartmann E, Hilpert M, *et al.*: **Direct observation of ultrafast collective motions in CO myoglobin upon ligand dissociation**. *Science* 2015, **350**:445–450.

107. Reddish MJ, Peng H-L, Deng H, Panwar KS, Callender R, Dyer RB: **Direct evidence of catalytic heterogeneity in lactate dehydrogenase by temperature jump infrared spectroscopy**. *J Phys Chem B* 2014, **118**:10854–10862.

108. Kraut DA, Carroll KS, Herschlag D: **Challenges in enzyme mechanism and energetics**. *Annu Rev Biochem* 2003, **72**:517–571.

109. Poelwijk FJ, Krishna V, Ranganathan R: **The context-dependence of mutations: a linkage of formalism**. *PLoS Comput Biol* 2016, **12**:e1004771.

110. • Yang G, Anderson DW, Baier F, Dohmen E, Hong N, Carr PD, Kamerlin SCL, Jackson CJ, Bornberg-Bauer E, Tokuriki N: **Higher-order epistasis shapes the fitness landscape of a xenobiotic-degrading enzyme**. *Nat Chem Biol* 2019, **15**:1120–1128.

Employs ancestral reconstruction and higher-order mutagenesis to understand the recently-evolved phosphotriesterase activity of methyl-parathion hydrolase (MPH). Only five spatially clustered mutations (none at the active site) converted a dihydrocoumarin hydrolase to an MPH. Higher-order epistasis accounted for only <1% (5-fold) of the ~1000-fold net MPH activity gain, suggesting promiscuous activity can be greatly enhanced without strongly epistatic networks, but evolutionary trajectories were constrained by epistasis among intermediates.

111. Sailer ZR, Harms MJ: **Molecular ensembles make evolution unpredictable**. *Proc Natl Acad Sci U S A* 2017, **114**: 11938–11943.

112. •• Morrison AJ, Wonderlick DR, Harms MJ: **Ensemble epistasis: thermodynamic origins of non-additivity between mutations**. *Genetics* 2021, **219**(1), iyab105, https://doi.org/10.1101/2020.10.14.339671.

Presents an analytical framework for predicting and understanding epistasis based on conformational ensembles. The authors find that the presence of multiple protein substates with differing functional properties, along with differential effects on substate occupancy upon mutation, can account for widespread epistasis in biology.

113. Carter P, Wells JA: **Dissecting the catalytic triad of a serine protease**. *Nature* 1988, **332**:564.

114. Wells JA: **Additivity of mutational effects in proteins**. *Biochemistry* 1990, **29**:8509–8517.

115. Sunden F, Peck A, Salzman J, Ressl S, Herschlag D: **Extensive site-directed mutagenesis reveals interconnected functional units in the alkaline phosphatase active site**. *eLife* 2015, **4**, e06181.

116. •• Pinney MM, Mokhtari DA, Akiva E, Yabukarski F, Sanchez DM, Liang R, Doukov T, Martinez TJ, Babbitt PC, Herschlag D: **Parallel molecular mechanisms for enzyme temperature adaptation**. *Science* 2021, **371**, eaay2784.

Describes simple molecular mechanisms accounting for thermoadaptation of activity and stability in a mesophilic and a thermophilic ketosteroid isomerase (KSI), almost fully accounted for by a single residue change at the active site. Through phylogenetic comparisons of ~2000 classes of homologous enzymes across ~5800 organisms, the authors found 1000s of examples of parallel changes in temperature adaptation, indicative of adaptive changes from small numbers of residues and limited epistasis.

117. • Russ WP, Figliuzzi M, Stocker C, Barrat-Charlaix P, Socolich M, Kast P, Hilvert D, Monasson R, Cocco S, Weigt M, *et al.*: **An evolution-based model for designing chorismate mutase enzymes**. *Science* 2020, **369**:440.

Direct coupling analysis, using first and second-order coupling terms from an alignment of extant chorismate mutase orthologs, was used as a generative model for non-natural sequences. More than 1000 artificial designed mutases were assayed with a competitive growth and deep-sequencing protocol, and nearly half (up to 80% sequence divergence) were apparently active, underscoring the importance of low-order coupling terms in specifying enzyme function, at least for this enzyme that is at the lower end in the range of catalytic rate enhancements.

118. Zhou N, Jiang Y, Bergquist TR, Lee AJ, Kacsoh BZ, Crocker AW, Lewis KA, Georghiou G, Nguyen HN, Hamid MN, *et al.*: **The CAFA challenge reports improved protein function prediction and new functional annotations for hundreds of genes through experimental screens**. *Genome Biol* 2019, **20**:244.

119. Andreoletti G, Pal LR, Moult J, Brenner SE: **Reports from the fifth edition of CAGI: the critical assessment of genome interpretation**. *Hum Mutat* 2019, **40**:1197–1201.